

Growth of ^4He -Crystals at mK-Temperatures

J. P. Ruutu,¹ P. J. Hakonen,¹ A. V. Babkin,¹ A. Ya. Parshin,^{1,*}
and G. Tvalashvili²

¹Low Temperature Laboratory, Helsinki University of Technology,
Espoo, FIN-02015 HUT, Finland

²Physikalisches Institut, Universität Bayreuth, D-95440 Bayreuth, Germany

(Received October 24, 1997; revised February 20, 1998)

*Liquid-solid interface of ^4He has been investigated down to mK-temperatures using an optical interferometer in combination with a sensitive pressure gauge. The **c**-facets with 5–100 screw dislocations/cm² grew with spiral growth which can be understood by including inertial terms and localization of steps to the standard theory. Crystals without screw dislocations revealed two novel growth mechanisms. At growth rates >1 nm/s, these high-quality crystals grew in a burst-like manner, creating abruptly 200–2000 new atomic layers. At rates below 0.5 nm/s, the **c**-facet revealed slow, continuous growth. Studies of **a**-facets yielded a velocity vs. pressure dependence which can be explained by spiral growth. The shape of the **c**-facet was monitored down to 2 mK without any evidence of the freezing of kinks. Pressure measurements down to our minimum temperature did not show any anomalies connected with the supersolid transition. Indications of new faceting transitions were not observed down to 2 mK.*

1. INTRODUCTION

Solid ^4He provides an excellent opportunity to study liquid-solid interfaces.^{1–3} Typically, growth of an interface is affected by the bulk properties since mass and heat flows are the limiting factors. However, at low temperatures ^4He transports heat away very fast and the latent heat of fusion is almost zero. As a result the interface can relax very quickly and it is possible to measure directly its equilibrium properties. ^4He is also an outstandingly pure substance since all other elements are frozen out except for ^3He .

The growth of an atomically rough surface of ^4He has shown extremely high rates, especially at very low temperatures.^{4–8} On the other

*Present address: P. L. Kapitza Institute for Physical Problems, ul. Kosygina 2, 117334 Moscow, Russia.

hand, the existence of atomically smooth surfaces, facets, has made it possible to study growth mechanisms which are based on the movement of elementary steps on top of a flat surface. The growth rates of facets are considerably smaller than those of the rough parts, which reflects the problems in placing new atoms on smooth surfaces. At high temperatures near the roughening transition, it is possible to nucleate terraces thermally. This growth mechanism has been studied on the *c*-facets at temperatures above 1 K by Wolf *et al.*⁹ and later by Gallet *et al.*¹⁰ In the former work, *a*-facets were also studied down to 70 mK. The experiments showed that screw dislocations were responsible for the growth far below the roughening temperature. More recently, Tsybalenko has measured the growth of both *c*- and *a*-facets in the temperature range of 0.5–1.5 K.¹¹ He assigned his results to the spiral growth from Frank-Read sources influenced by surface defects.

The classical picture of spiral growth predicts a facet velocity proportional to the driving pressure squared. However, this prediction is not necessarily valid any more at low temperatures when the mobility of steps becomes high. At large growth rates one has a situation where the step velocity starts to be on the order of the sound velocity. In this case, the classical picture of spiral growth breaks down. We have studied the growth of *c*-facets under such conditions and found clear deviations from the classical behavior. We present a model which is able to account for the new features of the spiral growth.

Before the present experiments, performed at temperatures 2–250 mK, the only observed growth modes of facets were the thermal nucleation of terraces and the spiral growth induced by screw dislocations.⁹ We have now been able to nucleate and study crystals which do not have any screw dislocations ending on the *c*-facet. In this situation the spiral growth is not possible and the overpressure required for terrace nucleation becomes large at low temperatures. In our work, however, two new growth mechanisms were found in such crystals.

Minimum temperatures in optical investigations of solid ⁴He have typically been limited to about 20 mK,¹² because of a sizeable heat leak due to infrared radiation through optical windows. By utilizing an interferometer with a cooled CCD-sensor we have now extended optical studies of ⁴He crystals down to 2 mK. One of the main motivations of our work was to study the growth of facets at mK-temperatures where the mobilities of elementary steps were expected to be high. Moreover, we wanted to monitor the crystal shape in order to look for new faceting transitions.

This paper is organized as follows: Sec. 2 describes the theoretical background of the shape and growth of ⁴He crystals. A modified theory of spiral growth, including the mass of a step and the decrease of step

mobility at large driving forces, is described. We also discuss possible effects of the critical velocities due to the Cherenkov emission of phonons and rotons. The experimental setup is discussed in detail in Sec. 3 as well as the methods for analysis of interferometric images and other topics of experimental techniques. We give a detailed description of our measurements¹³ on the **c**-facet growth in Sec. 4, covering both the spiral growth and the growth modes in the absence of screw dislocations. The effect of ^3He impurities on the growth was studied briefly by adding ^3He to the sample. We also present data on the growth of **a**-facets. In the end of Sec. 4 we describe our attempts to observe supersolid behavior as well as to see freezing of kinks at the lowest temperatures.

2. THEORETICAL BACKGROUND

2.1. Equilibrium Shape of Crystals

The shape of a crystal is determined by the surface energy α . The total surface free energy is

$$E = \int_S \alpha(\theta, \phi) dS \quad (1)$$

integrated over the surface S of the crystal. The minimization of E at constant volume yields the equilibrium shape of the crystal. One obtains in the 1D case

$$\frac{\tilde{\alpha}(\theta)}{R(\bar{r})} = F/a \quad (2)$$

where $\tilde{\alpha} = \alpha + d^2\alpha/d\theta^2$ is the surface stiffness, $R(\bar{r})$ is the radius of curvature at the position \bar{r} , a is the lattice spacing and the supercooling force is defined as³

$$F = a \frac{\rho_s - \rho_l}{\rho_l} \Delta p \quad (3)$$

Here $\Delta p = p - p_{eq}$ is the deviation from the equilibrium liquid pressure p_{eq} for a flat interface and ρ_l and ρ_s are the densities of the liquid and solid phases, respectively.

The surface energy α may have a cusp when the angle θ between the surface and some lattice plane of the crystal becomes zero. This leads to a discontinuity of the first derivative α' and to the appearance of atomically

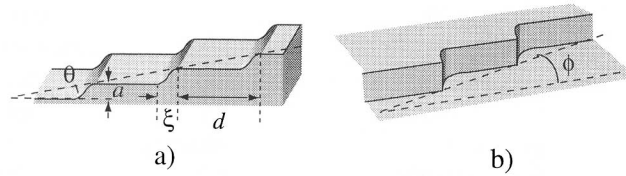


Fig. 1. (a) Vicinal surface. (b) Kinks on a step inclined by an angle ϕ with respect to a crystalline axis.

smooth planes, facets. This occurs at some characteristic temperature T_R , when thermal fluctuations become small enough. Since it is possible to define various lattice planes in a crystal, there may be many faceting transitions; in principle one for every orientation, corresponding to rational Miller indices. Thus, with decreasing temperature the surface of a ^4He crystal has an increasing number of facets which are connected by curved parts.

Three different facets have been found in ^4He crystals. The first facet observed was the **c**-facet (0001), the basal plane of the hexagonally symmetric ^4He crystal with the highest critical temperature $T_{R1} = 1.3 \text{ K}$.^{4, 14, 15} When lowering the temperature further, six **a**-facets ($1\bar{1}00$) appear at $T_{R2} = 0.9 \text{ K}$.^{4, 15} Below $T_{R3} = 0.3 \text{ K}$, **s**-facets ($1\bar{1}01$) are formed between the **c**- and **a**-facets.¹⁶ At lower temperatures, more transitions are expected to exist but these, however, have not yet been observed.

A surface, which is tilted by a small angle θ with respect to a high symmetry axis, is important in understanding the basic properties of crystal surfaces. These so called vicinal surfaces consist of atomically smooth terraces separated by transition regions, steps. In a step the surface height changes by one lattice spacing a over the step width W , as shown in Fig. 1a. The free energy of a step per unit length, β , has been measured for **c**-facets by Rolley *et al.*¹² who obtained, at temperatures well below 1 K, $\beta/a = 1.1 \cdot 10^{-2} \text{ erg/cm}^2$ which is pertinent to our experiments with helium of natural purity. When the inclination angle θ becomes large enough, so the distance between steps becomes on the order of their width, it is not possible to define separate terraces any more. In this limit, the interface state is called atomically rough.

The concept of steps and terraces is also useful when the properties of facets are considered. Equilibrium size of a facet, for example, depends on the step energy β and on the supercooling force F . This can be seen by considering the energy of a new layer on the facet. For a horizontal **c**-facet, neglecting gravity, the energy of a disc with radius R is

$$\Delta E(R) = 2\pi R\beta - \pi R^2 F \quad (4)$$

For a facet in equilibrium one obtains the radius

$$R_{eq} = \frac{2\beta}{F} \quad (5)$$

If the supercooling force is determined by the curved part of the crystal with the radius of curvature R_r so that $2R_r \sim D$, the size of the crystal, then $R_{eq}/D \sim (\beta/a)/\alpha \sim 0.05$. Hence, the c-facets are expected to cover only small sections of the crystal interface. On large crystals with smoothly curved rough parts the c-facets become large. For example, $\Delta p \sim 1 \mu\text{bar}$ corresponds to a facet with the diameter of $\sim 0.5 \text{ cm}$.

The facet, on the other hand, collapses below a critical facet size. The maximum energy of Eq. (4) is obtained at the critical radius

$$R = R_c = \frac{\beta}{F} \quad (6)$$

which corresponds to a local metastable state, where the supercooling force is balanced by the line tension. When the radius $R < R_c$ the facet collapses whereas above R_c the facet continuously expands towards R_{eq} . However, one should notice that, in order to reach the equilibrium size, vertical movement of the horizontal facet is needed. If the facet is not able to move vertically, it expands sideways until the supercooling force is balanced by step-step interactions at the edge of the facet which then has a metastable radius.

Similar to a vicinal surface, a step may be tilted by an angle ϕ with respect to a crystalline axis, if it has "kinks" at which it shifts by one lattice spacing as shown in Fig. 1b. There exist kinks of two signs according to the direction of the change on the step. In classical statistical mechanics kinks may be considered as point defects, thermally excited on linear steps (strictly speaking, only pairs of kinks of opposite signs can be thermally excited). A kink has an activation energy ε_k and a width $\sim W$ of the transition region.³ The order of magnitude of the kink energy can be estimated by assuming that the extra length of the step due to a kink is $\sim a^2/W$.^{3, 12} Thus one obtains an estimate for the kink energy

$$\varepsilon_k \sim \beta \frac{a^2}{W} \quad (7)$$

Using $W \approx 10a$,¹² we obtain $\varepsilon_k/k_B \approx 10 \text{ mK}$.

A finite kink energy will influence the circumference of a facet. The orientation of a step determines the number of kinks and, consequently, the

change in the step energy $\Delta\beta(\phi)$. For a step with the length L_s , the number N_k of kinks can be estimated as $(L_s/a) \sin \phi$ ($\phi > 0$). Thus, $\Delta\beta(\phi)$ becomes

$$\Delta\beta(\phi) \sim N_k \varepsilon_k = \frac{L_s}{a} \sin \phi \varepsilon_k \quad (8)$$

The ratio of $\Delta\beta_{\max}$ to the step energy is ~ 0.05 , which means that the expected deformation of the facet shape is weak.

Note that the above picture neglects the effect of quantum delocalization of point defects at low temperatures. Quantum-mechanical considerations¹⁷ imply the possibility of zero-point kinks with exactly zero activation energy.

2.2. Facet Growth of Helium Crystals

Atomically rough surfaces grow rapidly while facets grow slowly. This difference reflects the difficulties in placing new atoms on atomically smooth facets. Therefore, to induce growth, some mechanism is required for the creation of sites where new atoms can stick to. One possibility is the thermal nucleation of terraces. Near the roughening temperature thermal fluctuations are big enough, compared with the potential barrier for the creation of a new terrace in Eq. (4). The nucleation of terraces on c-facets has been studied by Wolf *et al.* at the temperatures 1.13–1.25 K,⁹ and later by Gallet *et al.*¹⁰ These temperatures were close to the first roughening temperature $T_{R1} = 1.3$ K where β vanishes. They concluded that the thermal nucleation of terraces explained their results on the growth of c-facets.

2.2.1. Classical Spiral Growth

At lower temperatures β increases while thermal fluctuations become weaker. Therefore, the thermal nucleation of terraces is not effective any more and one needs a new mechanism. This may be the classical spiral growth, induced by screw dislocations. When going around a dislocation line, the surface height changes by the length of the Burgers vector. Thus, such a dislocation produces an elementary step on the facet (a pair of steps of the same sign on a c-facet of an hcp-crystal, since in this case the Burgers vector is twice the step height a). Two screw dislocations with opposite signs, joined by a step, form a Frank-Read source. When excess pressure is applied, the step between the dislocation lines of a Frank-Read source starts to bulge outwards. The step spreads around and behind the dislocation lines until a complete new terrace has been created. This terrace starts

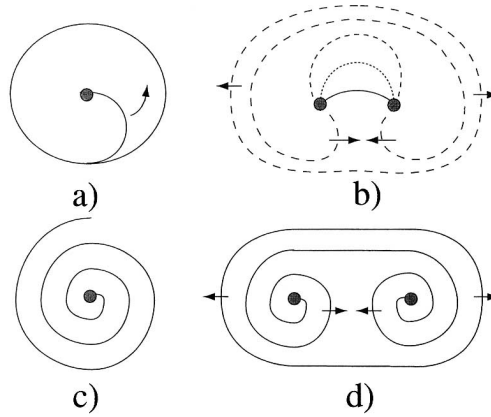


Fig. 2. Spiral growth induced by screw dislocations. Growth of a single dislocation under a small excess pressure (a) and of a Frank-Read source (b). At higher growth rates the dislocation winds around itself to produce a spiral as shown for a screw dislocation (c) and for a Frank-Read source (d).

to expand over the facet as shown in Fig. 2b. At higher growth rates, the step emerging from the dislocation becomes even more curved and finally its shape becomes a spiral as shown in Fig. 2c and 2d.

A characteristic feature of the spiral growth is that the step in a Frank-Read source doesn't move before the excess pressure Δp becomes bigger than a threshold pressure Δp_c . This threshold is obtained from the force balance acting on the step according to Eq. (6). The step starts moving when the radius of curvature becomes smaller than half of the distance l_d between the dislocation lines. Using Eq. (6) with $R = l_d/2$, together with Eq. (3), one obtains for the critical pressure¹⁸

$$\Delta p_c = 2 \frac{\rho_l}{\Delta \rho} \frac{\beta}{l_d a} \quad (9)$$

where $\Delta \rho = \rho_s - \rho_l$. According to this formula the threshold pressure yields the distance between the dislocation lines of a Frank-Read source. When there are several screw dislocations of opposite signs ending on the facet, the steps are formed between neighboring dislocations in order to minimize their length and energy. Hence, a measurement of the threshold gives an approximate value for the distance between neighboring screw dislocations and, thereby, characterizes the quality of the crystal.

In order to find the v vs. Δp dependence of the spiral growth one has to start from the force balance acting on a step (Eq. (6)) supplemented with a term containing the frictional force in a steady-state situation¹⁹

$$\frac{\beta}{R(\bar{r})} + \frac{v_s}{\mu} = F \quad (10)$$

where $R(\bar{r})$ is the local radius of curvature and F is the step driving force, which is identical to the supercooling force given by Eq. (3). The second term on the left side includes the step mobility μ defined by

$$\mu = \frac{v_s}{F} \quad (11)$$

The solution of Eq. (10) is a growth spiral with the asymptotic spacing¹⁹

$$d = \frac{2\pi}{\Lambda} \frac{\rho_l}{\Delta\rho} \frac{\beta}{a\Delta p} \approx 19 \frac{\rho_l}{\Delta\rho} \frac{\beta}{a\Delta p} \quad (12)$$

where Λ is an eigenvalue of Eq. (10). The facet velocity v and the step velocity v_s of the spiral are connected by

$$v = \frac{a}{d} v_s \quad (13)$$

where d is the distance between the spiral arms (in the case of c-facets of hcp-crystals the value of v is two times larger). Since steps cannot cross each other the growth of Frank-Read sources is not cumulative. On the other hand, the time needed for a Frank-Read source to make one new layer, $\tau = d/v_s$, is not affected by the distance to other sources either. As a result, the growth velocity of a facet does not depend on the density of dislocations except for the threshold.

According to Eqs. (11), (12) and (13) the facet velocity becomes

$$v = \left(\frac{a\Delta\rho}{\rho_l} \right)^2 \frac{a\mu}{19\beta} \Delta p^2 \quad (14)$$

This Δp^2 dependence on pressure, together with the growth threshold, is a distinct feature of classical spiral growth.

According to theoretical estimations, based on the concept of quantum kinks and steps,^{17,20} the step mobility μ may increase to infinity at low temperatures. In other words, the step velocity may be very high even at rather small driving forces. In our experiments facet velocities have been

measured to be on the order of $v = 10 \mu\text{m/s}$ with $\Delta p = 2 \mu\text{bar}$ (see Sec. 4.3). Using Eqs. (12) and (13) one obtains a step velocity of $v_s \sim 300 \text{ m/s}$. This value is close to the sound velocity in ^4He .²¹ Thus, it is obvious that modifications have to be made to the regular theory of spiral growth. In the following, we assume that steps on the facets of helium crystals are essentially quantum objects, with a high density of zero-point kinks.

2.2.2. Modified Theory of Spiral Growth

Unlike in the classical theory of spiral growth, we have to take into account the step inertia which dominates the equation of step motion, when the energy dissipation is low. The step mass m comes mainly from the kinetic energy of the superflow which transfers helium atoms from liquid to the solid phase. With this modification Eq. (10) can be written as

$$m \left(\frac{\partial v_s}{\partial t} + v_s \frac{\partial v_s}{\partial n} \right) = F - \frac{\beta^*}{R(\bar{r})} - \frac{1}{\mu} v_s \quad (15)$$

where m is the effective mass of a step per unit length, n is normal to the step, and $\beta^* = \beta + mv_s^2/2$ denotes the step energy including the kinetic energy; the term $v_s \partial v_s / \partial n$ has exactly the same origin as a similar term in the Euler equation of classical fluid mechanics. Note that we need to use β^* instead of β in order to make Eq. (15) consistent with energy conservation.

At small driving forces F , the step mobility is some temperature-dependent coefficient μ_0 , defined by collisions of the step with phonons in the liquid.²⁰ At sufficiently large F , however, this process cannot provide the necessary energy dissipation for a steady drift of a step, and a new mechanism should be switched on, which then puts a limit to the step speed. One of the possible mechanisms of this kind is caused by the localization of kinks at large driving forces. Quantum kinks on a step were originally introduced as narrow-band quasiparticles.¹⁷ Such particles may drift in an external field only if there is a way to release their excess kinetic energy. Since the movement of a step is governed by the motion of kinks, the step may be localized by a strong external field, in accordance with other low-dimensional quantum systems with narrow-band quasiparticles.²² In the regime of localization, the step drift velocity can be expressed as $v_s = 1/(\eta F)$ where η is a new characteristic parameter of the energy dissipation.

To obtain a rough estimate of the value of η , we have used a simple model of a step as an one-dimensional lattice gas of quantum kinks of only one sign. Kinks are quasiparticles with average density n_k on the step and the width of their energy band $\Delta_k \ll \Theta_D$, the characteristic Debye

temperature. Due to the nonzero difference $\rho_s - \rho_l$ each kink moving along the step produces a velocity field in the liquid $\vec{v}_l(\vec{r})$. The main term in the kink-phonon interaction may be written in the form $\delta\rho_l v_l^2/2$, where $\delta\rho_l$ is the variation of the liquid density due to phonons. The energy transfer from kinks to phonons is a result of inelastic kink-kink collisions with emission of phonons, which can be calculated using the standard perturbation theory. Assuming that in the regime of localization the step is “hot” as compared with the phonon bath and that the average kinetic energy of a kink is of order Δ_k , we obtain

$$\eta = \frac{A}{\rho_l n_k^2 a^6} \left(\frac{\rho_l}{\Delta\rho} \right)^4 \frac{\hbar^3 \Theta_D^5}{\Delta_k^8} \quad (16)$$

where A is rather complicated integral, which can be estimated as $A \sim 10^3$. Note that our model is certainly oversimplified (we neglect kink-kink interactions, the creation and annihilation of pairs of opposite kinks, etc.) and that it is able to give a rough estimate of η at best. Therefore, in our analysis of Eq. (15) over different regimes we used the simplest interpolation formula

$$\frac{1}{\mu} = \frac{1}{\mu_0} + \eta F^2 \quad (17)$$

Within our rough model, a more accurate estimation of μ in the intermediate regime seems not to make real sense.

In the case of steady rotation at an angular frequency ω , the shape of a spiral step in polar coordinates centered on the dislocation is given by a function $\phi(r)$ which must be regular at all r . The growth velocity of the facet itself is governed solely by ω since $v = a\omega/2\pi$. Stationary solutions of Eq. (15) can be obtained, generally speaking, only numerically. However, in all the special cases of interest this equation has simple analytical solutions. The character of these solutions depends basically on the value of a dimensionless parameter

$$\gamma = \frac{mF^2\mu^2(F)}{\beta} \quad (18)$$

At high temperatures, when $\mu_0 \ll \beta\eta/m$, this parameter is small ($\gamma \ll 1$) at all values of F and Eq. (15) yields

$$v = \Lambda \frac{\mu_0 a}{2\pi\beta} \frac{F^2}{1 + \mu_0\eta F^2} \quad (19)$$

This result recovers the regular F^2 dependence at small F while it shows saturation of the growth velocity at large F . In the opposite limit of low temperatures there is a range of driving forces, $\mu_0\eta \gg 1/F^2 \gg \beta\eta^2/m$, where $\gamma \gg 1$. Then we obtain a linear dependence

$$v = \frac{aF}{2\pi \sqrt{2m\beta}} \quad (20)$$

while outside this domain we return to Eq. (19). The physical reason for this unusual “inertial” growth regime is that the inertial terms dominate in Eq. (15) at small r , where the step characteristics are formed; as a result the growth velocity does not depend on the step mobility. In this case we have a flow of energy from the center of the spiral to the facet border rather than energy dissipation on the facet itself. If the facet size is large enough, the step velocity eventually reaches its maximum velocity, defined by Eq. (11), and the asymptotic spacing of the spiral arms becomes

$$d = 2\pi\mu \sqrt{2m\beta} \quad (21)$$

Figure 3 illustrates the results of a numerical solution of Eq. (15) with different values of the step parameters.

One more reason for nonlinear behavior of μ might be caused by the Cherenkov emission of rotons and phonons by a moving step, as its speed

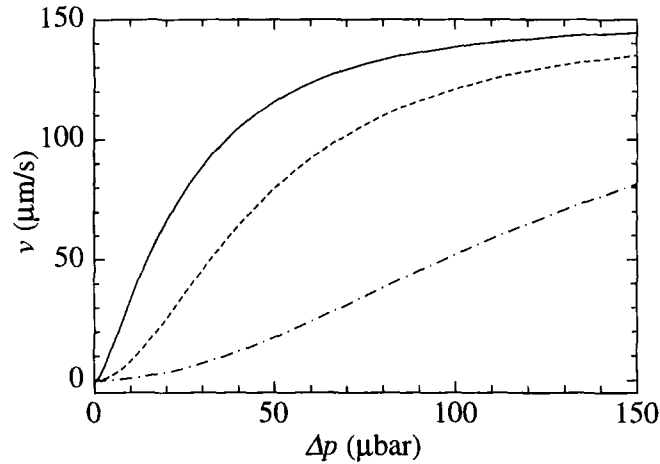


Fig. 3. Numerically calculated v vs. Δp from Eqs. (13), (15) and (17): $\mu_0 = 10^{12}$ s cm/g (solid line), $\mu_0 = 10^{11}$ s cm/g (dashed line) and $\mu_0 = 10^{10}$ s cm/g (dash-dotted line) with $\eta = 500$ and $m = 5 \cdot 10^{-18}$ g/cm.

exceeds the corresponding critical velocities (the roton phase velocity v_r , the sound velocity in the liquid c_l or in the solid c_s). In this case Eq. (17) changes into

$$\frac{1}{\mu} = \frac{1}{\mu_0} + \eta F^2 + \kappa(v_s) \quad (22)$$

where the additional friction $\kappa(v_s)$ is practically zero below a threshold velocity v_c and increases very fast above it. In order to estimate this additional friction, we have calculated the flow of energy from a moving step in the hydrodynamical approximation; the “weak coupling” model³ was used to describe the profile of the step. The emission of phonons into the liquid yields

$$\kappa(v_s) = \frac{1}{4\pi^4} \frac{(\Delta\rho)^2 a^2 c_l}{\rho_l \xi} \sqrt{2 \left(\frac{v_s}{c_l} - 1 \right)} \quad (23)$$

where ξ is the correlation length which defines, in particular, the effective width of the step as $W \approx 4\xi$.¹² Numerical estimations show that this “Cherenkov” friction may be very strong: $\kappa\mu_0 \gg 1$ above v_c at all temperatures below 0.3–0.5 K. The Cherenkov emission of phonons into the crystal, due to elastic stresses produced by a step,²³ gives an additional friction which is roughly of the same order. Finally, the roton contribution may be written, within an order of magnitude, as

$$\kappa(v_s) \sim \frac{1}{2\pi^2} \frac{(\Delta\rho)^2 a^2 \Delta_r}{\rho_l \hbar} \frac{\sqrt{m_r \Delta_r}}{p_0} \exp\left(-\frac{\pi\xi p_0}{\hbar}\right) \left(\frac{v_s}{v_r} - 1\right) \quad (24)$$

where Δ_r , p_0 and m_r are the energy gap, the momentum, and the mass of a roton, respectively. Due to the exponential factor in Eq. (24) this contribution appears to be very sensitive to the value of ξ and quite small compared with Eq. (23): using $\xi = 2a$,¹² we obtain $\pi\xi p_0/\hbar \sim 38$.

It is necessary to emphasize here that radiation processes described by Eq. (16) and Eqs. (23), (24) are quite different. The first type of radiation is active when the step is hot, i.e., its internal degrees of freedom (kinks) are hot as compared with the phonon-roton bath. In contrast, the Cherenkov radiation appears even when a cold step as a whole is moving sufficiently fast relative to the bulk liquid or solid.

In order to analyze possible effects of the above critical velocities, we have studied the solutions of Eq. (15) obtained with a step mobility which suddenly falls down to a very small value at some critical velocity v_c . In

this case we have one more dimensionless parameter $M = mv_c^2/2\beta$. If $M > 1$ or $v_c > F\mu$, where μ is the step mobility below the threshold, the growth velocity does not depend on v_c and we return to the previous solutions, i.e., Eq. (19) or Eq. (20). If $M < 1$ and μ is sufficiently high, $\mu \gg v_c/F$, we obtain for the velocity

$$v = \frac{av_c}{2\pi(1+M)\beta} F \quad (25)$$

By comparing with Eq. (20) we see that the step mass and the step critical velocity play very similar roles in the spiral growth, which makes the interpretation of experimental data more complicated.

2.3. Supersolid

In addition to zero point kinks on the liquid-solid interface, solid ^4He may have zero-point excitations in the bulk. These bulk excitations, for example vacancies, are supposed to form a Bose-condensate, a supersolid, below a critical temperature T_c .²⁴⁻²⁶ The supersolid transition is expected to manifest itself as an anomaly in the melting curve, like the superfluid transition in ^3He . The difficulty is that the pressure variation due to the Bose-Einstein condensation is extremely small at the expected density of vacancies. The predictions for the slope of the melting curve across the supersolid transition are²⁶

$$\frac{dp}{dT} = \begin{cases} n_v R & T \gg T_c \\ 0.51 n_v R & T \leq T_c \end{cases} \quad (26)$$

where R is the gas constant and n_v is the density of vacancies participating in the condensation. The critical temperature is

$$T_c = \left(\frac{\hbar^2}{2\pi m k_B} \right) \left(\frac{n_v}{2.612} \right)^{2/3} \quad (27)$$

There are also other temperature-dependent contributions to the melting pressure, for example due to ^3He impurities. At low temperatures the impurities behave as an ideal gas governed by the usual equation of state $pV = n_3 RT$. Taking a derivative one obtains $dp/dT = n_3 R/V$. Using a typical ^3He concentration 10^{-7} one obtains $0.4 \mu\text{bar/K}$, which, however, is beyond the resolution of our pressure gauge (see Sec. 3).

3. EXPERIMENTAL TECHNIQUES

3.1. Experimental Setup

A schematic illustration of our two-beam optical interferometer is displayed in Fig. 4. Coherent illumination is produced using a He-Ne laser, located at room temperature. The light is focused to a single-mode optical fiber that goes via the He-bath and enters the vacuum can of the cryostat through a Stycast 1266 feedthrough. The beam is expanded with two lenses to a parallel beam which is taken with a pair of mirrors vertically through the sample cell. Most of the light passes the top and bottom windows of the cell and the sample itself, after which the illumination is guided out of the coldest parts of the cryostat. This light is absorbed by a black surface thermally anchored to the still. About one ppm of the light is reflected from

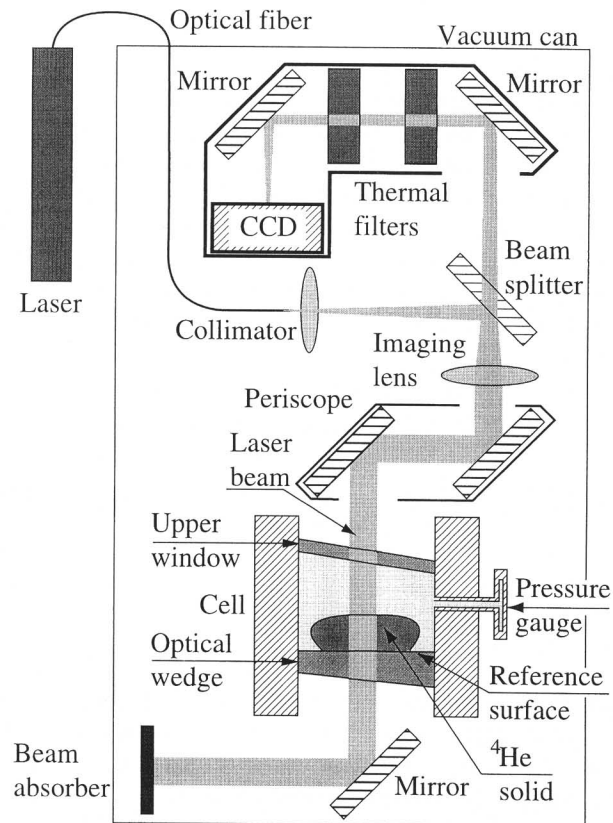


Fig. 4. Experimental setup.

the liquid-solid interface and ~ 100 ppm from the anti-reflection coated reference surface on top of the lower window. These two reflections interfere with each other and they are focused to a cooled CCD-sensor.

We use a slow scan CCD-camera Star 1 which takes 12-bit grayscale images.²⁷ The sensor has to be kept around $T \approx 60$ K in order to maintain the mobility of charge carriers. Two thermal filters have been installed in front of the sensor to eliminate thermal radiation. The image is read from the sensor to the control unit of the camera and transferred to a computer for storage and digital image processing. The control unit has a memory for one 12 bit image of the size $576(\text{H}) \times 384(\text{V})$ pixels.

Pressure inside the cell is measured using a capacitive gauge of Straty-Adams type,²⁸ installed on the nuclear stage of the cryostat. The gauge, made of BeCu, has a membrane with the diameter of 9 mm and the thickness of 0.3 mm which is less than the thickness of 1 mm used in the conventional design.²⁸ The gauge is connected to the liquid volume of the cell using a CuNi-tube of 1 mm in diameter. The pressure sensitivity of the gauge is 6 pF/bar. The capacitance is measured using a commercial capacitance bridge²⁹ which yields a pressure resolution of $0.3 \mu\text{bar}$.

The sample cell, made of copper, is installed 10 cm above the top plate of the nuclear stage in order to fit a mirror below. The inner diameter of the cell is 17 mm and its height is 18 mm so that the experimental volume is 4.1 cm^3 . The top and bottom of the cell are optical-grade fused silica windows which have anti-reflection coatings on both surfaces. The upper window is tilted by 2° with respect to the cylinder axis in order to prevent light reflected from it to reach the CCD-sensor. For the same reason the bottom window is a wedge aligned so that only the reflection from its upper surface, used as the reference plane, hits the sensor. The optical volume is connected to the top of the nuclear stage with a filling tube having an inner diameter of 4 mm. Built into the top of the nuclear stage we have a sintered silver heat exchanger with the nominal surface area of 114 m^2 for cooling down ^4He . The cell is connected to the nuclear stage with three supporting legs, one of which provides good thermal sinking via a conical contact surface.

The thermal time constant $\tau = RC = C/K$ of the experimental setup was estimated in order to approximate the minimum temperature of the sample. The heat capacity of ^3He impurities, $C_3 = (3/2) x_3 R \text{ J/K}$, dominates below 20 mK. Here $x_3 = 10^{-7}$ is the concentration of ^3He within the commercial ^4He that we used for our experiment. The heat conductivity of the ^4He liquid phase can be written as $K_l = 525 T^3 \text{ W/Km}$.³⁰ On the other hand, above the Fermi-temperature ($T_F = 0.05 \text{ mK}$ with $x_3 = 10^{-7}$) one obtains for ^3He impurities $K_3 = 3.8 \cdot 10^{-4} T^{1/2} \text{ W/Km}$. Above $T \sim 3 \text{ mK}$ the liquid ^4He starts to dominate the heat conductivity while at lower temperatures

the ^3He impurities conduct better. Multiplying these values by $A/l \sim 10^{-3}$ m, where A is the cross-section of the filling tube between the sinter and the cell and l is its length, one obtains the thermal conductivity of the liquid column. Hence, the time constant above a few millikelvin is

$$\tau_{>} = C_3/K_l = \frac{2.4 \cdot 10^{-7}}{T^3} K^3 s \quad (28)$$

and for the temperatures below

$$\tau_{<} = C_3/K_3 = \frac{3.3 \cdot 10^{-1}}{T^{1/2}} K^{1/2} s \quad (29)$$

Eqs. (28) and (29) show that the crossover between the two time constants occur around $T \sim 3$ mK being around $\tau \sim 5$ s.

The main heat leak to the sample comes from the illumination which is absorbed by the windows and transferred to the sample. We estimate that the illumination used at the lowest temperatures produced a heat leak of $\dot{Q} \sim 0.02$ nW. Using the thermal conductivity of the tube connecting the cell and the heat exchanger, we obtain a cooling capacity corresponding to this heat leak at $T \approx 2$ mK. Hence, according to the estimations of the thermal time constant τ and the heat leak \dot{Q} , we can expect the minimum temperature of the sample to be about 2 mK.

Temperature was measured either using a carbon resistor in the mixing chamber ($T = 20\text{--}300$ mK) or using a Pt-wire NMR thermometer installed on the top flange of the nuclear stage ($T = 0.3\text{--}70$ mK). The basic heat leak to the nuclear stage was around 30 nW and the pulsed illumination gave 0.02–6 nW extra depending on the pulsing frequency.

The fill line of the sample cell was connected to a room temperature ballast volume of 100 cm³. The temperature of the volume could be controlled using an electrical heater. By driving a sinusoidal current through the heater we were able to grow and melt the crystal periodically. The temperature of the ballast was measured using a Pt100-resistor. Typically the ballast was operated between 30–80°C. To ensure as fast cooling as possible the ballast volume was cooled with air flow.

3.2. Analysis Methods for Interferograms

In order to measure very small speeds of a growing c-facet we utilized the following method. First we imaged a small part of the facet at constant time intervals. From the image we resolved the phase of the interference lines utilizing a Fourier analysis method described by Kostianovski *et al.*³¹

Since the phase changed with the position of the c-facet, the trace of the facet height was obtained as a function of time. This method allowed us to measure growth rates of the facet down to 0.01 nm/s.

The Fourier analysis is illustrated in Fig. 5. First a background picture is subtracted from the raw image in order to make the interference lines

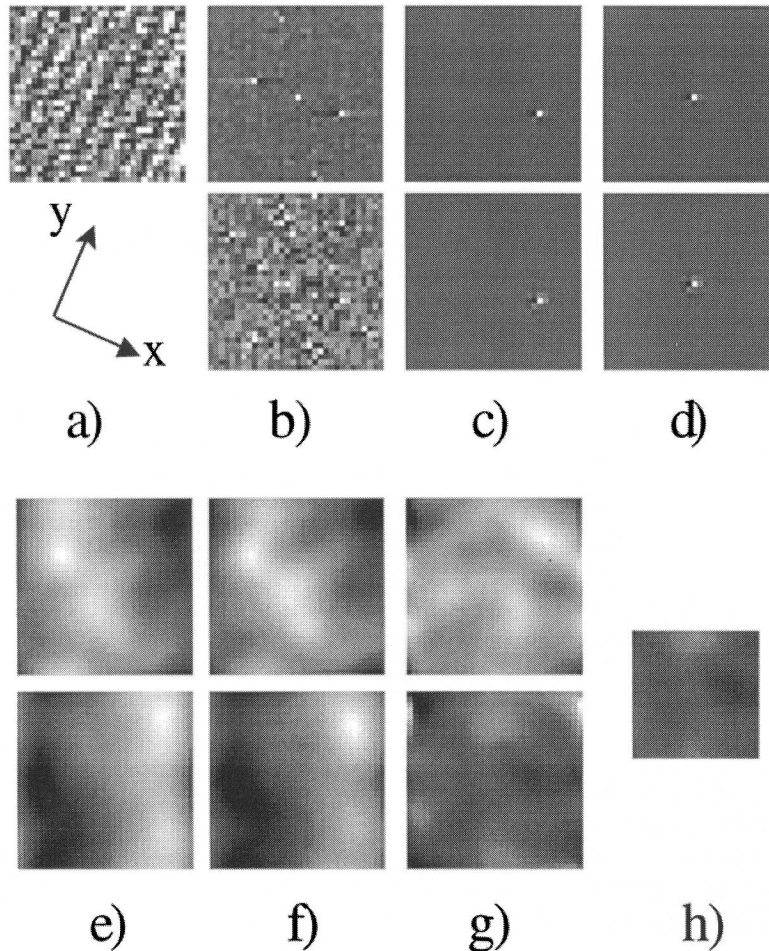


Fig. 5. Phase analysis using Fourier transformation in 2D. (a) An image $g(x, y)$. (b) Fourier-transformation $G(u, v)$ of $g(x, y)$ showing the real (upper) and imaginary (lower) components. (c) One of the side maxima is filtered with a Gaussian filter. (d) The side maximum is transferred to the center of the image. (e) An inverse Fourier-transformation yields $g'(x, y)$. (f) The reference $g'_0(x, y)$. (g) The result of the complex division g'/g'_0 . The upper image is the amplitude $c(x, y)$ and the lower one is the phase component $\Delta\phi(x, y)$. (h). The middle of the phase is averaged to obtain the phase difference. See text for more details.

more clear (a). The background is obtained taking several pictures from a growing or melting crystal with varying positions of the interference lines. Averaging these pictures one obtains an image containing the background without interference lines. The starting point for the analysis is the background-subtracted interferogram which, owing to straight interference lines along the y -axis, can be written as

$$g(x, y) = a(x, y) + 2b(x, y) \cos[\omega_0 x + \phi(x, y)] \quad (30)$$

where $\omega_0 = 2\pi/L$ is determined by the spacing L of the interference lines, $a(x, y)$ is a term coming from inhomogeneities of the optics and $b(x, y)$ is the spatial variation of the interference lines owing to the same reason. The y -axis has been chosen along the interference lines as seen in Fig. 5a. In an ideal situation the functions a and b would not depend on the position (x, y) , but this is not the case in our experimental images as seen in Fig. 5a.

The Fourier-transformation in 2D of Eq. (30) is given by

$$G(u, v) = A(u, v) + B(u, v) * [\delta(u - \omega_0) \delta(v) * P_0(u, v) + \delta(u + \omega_0) \delta(v) * P_0^*(-u, -v)] \quad (31)$$

where $P_0(u, v) = \mathcal{F}\{\exp[i\phi(x, y)]\}$, $A(u, v) = \mathcal{F}\{a(x, y)\}$ and $B(u, v) = \mathcal{F}\{b(x, y)\}$. The resulting image is complex with real (upper image) and imaginary (lower image) components as shown in Fig. 5b; since the function $g(x, y)$ is real, $G(u, v)$ is symmetric. The central maximum is the zero-order peak and the two side maxima are the first order peaks produced by the interference lines. Next, one of these side maxima is selected. In order to remove the higher order peaks and the zero-order peak, the image is filtered using a Gaussian window $W = \exp\{-[(u - \omega_0)^2 + v^2]/2\sigma^2\}$ positioned on the selected peak (c). The filtered peak is then shifted to the origin: the same procedure is done with the imaginary component. Fig. 5d shows the result. This filtered complex image is transformed by inverse Fourier transformation in 2D yielding a complex image $g'(x, y)$ as seen in Fig. 5e. This whole analysis is repeated with another image, yielding $g'_0(x, y)$ shown in Fig. 5f, which is used as a reference for the movement of the interference lines. In order to find the movement of the interference lines we perform a complex division

$$k(x, y) = \frac{g'(x, y)}{g'_0(x, y)} = c(x, y) \exp[i\Delta\phi(x, y)] \quad (32)$$

The amplitude component $c(x, y)$ is shown in the upper image of Fig. 5g while the phase difference $\Delta\phi(x, y)$ of the interference lines is shown in the

lower image. Taking an average over the central area of $\Delta\phi(x, y)$ shown in Fig. 5h, we obtain the phase difference of the lines $\Delta\phi_{ave}$ and, consequently, the movement of the facet from the formula

$$\Delta h = \frac{\lambda}{4\pi} \Delta\phi_{ave} \quad (33)$$

where λ is the wavelength of the illumination.

Our camera has a feature which allows the imaging of a small area of the sensor element instead of the whole array. The small images are stored to the memory that is normally used for one full frame. As a result one obtains a mosaic picture consisting of small images separated by a short time interval. The advantage is that the imaging rate can be increased from one picture every 9 seconds to one image every 0.4 seconds. We took typically sequences containing 198 images of 32×32 pixels. These mosaic images were analyzed in a Macintosh computer using a commercial image processing software IPLab produced by Signal Analytics.³² The subtraction of the background was made manually since the best lines were obtained by testing several different backgrounds. After this the first frame of the mosaic image was selected as the reference and the phase difference of the interference lines in the rest of the frames was extracted automatically using the Fourier analysis method. The processing of a typical mosaic image took about 20 minutes using a PowerMacintosh 7100 computer. The results obtained using this method for small growth rates are discussed in Sec. 4.2.

3.3. Calibrations for Mobility Measurements

It is not possible to use the interference lines for measuring movement of the c-facet at high growth rates. If the facet height changes between the successive frames by more than $\lambda/2$, one loses the count of the lines. Thus, at growth rates higher than $v \sim 0.5 \mu\text{m/s}$, we employed the hydrostatic pressure to measure the growth rate of the c-facet. As the height of a horizontal c-facet changes with Δh , the liquid pressure in the sample cell changes by

$$\Delta p_h = \rho_l g \Delta h \quad (34)$$

where ρ_l is the density of the liquid. However, during growth one has also a driving pressure Δp applied to the sample cell. Therefore, the pressure measured with the gauge is

$$\Delta p_g = \Delta p + \Delta p_h \quad (35)$$

These two components have to be separated from each other in order to obtain the facet mobility at the driving pressure Δp .

The functional form of the applied mass flow was calibrated when the cell did not contain any solid. The sinusoidal current of the ballast heater produced in the cell a periodically changing pressure which had a slightly steeper increasing than decreasing part. This distortion from a pure sinusoid was growing with the increasing drive amplitude. We found that the mass flow and consequently Δp_h due to the changing hydrostatic pressure was described well with a “tilted” sine-wave of the form

$$\Delta p_h = A \sin[2\pi ft + \alpha \sin(2\pi ft)] \quad (36)$$

where A is the amplitude, f is the frequency of oscillation and α is a parameter determining the amount of distortion. We calibrated α at different amplitudes of the periodic drive and used then these values in our analysis. At the largest drive we had $\alpha = 0.17$.

Figure 6 illustrates the mobility measurements. We made a fit of Eq. (36) using a fixed α (from the calibration) and f (the drive). The amplitude A was a free parameter of the fit. The fitting points were on the decreasing

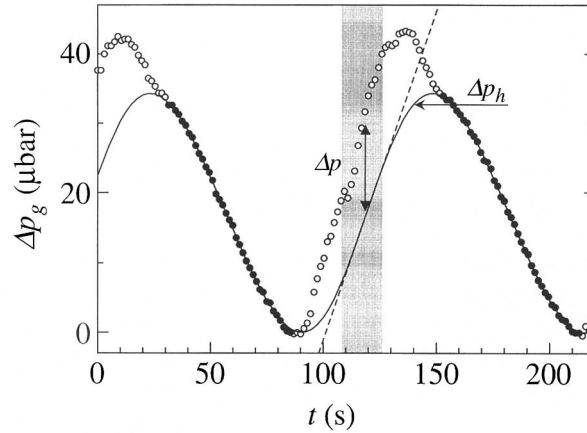


Fig. 6. Pressure Δp_g of the sample as a function of time t measured with the capacitive gauge during periodic growth and melting of the c-facet at $T = 20$ mK; the change of the facet height is 2 mm. The zero of Δp_g is fixed to the minimum pressure over the period. The solid curve shows the fitted hydrostatic pressure Δp_h according to Eq. (36) using filled circles. The parameter α , used for the fit, was obtained from the calibration. The dashed line indicates the linear fit to Δp_h over the shaded time interval which yields the facet velocity v according to Eq. (34).

parts of the oscillation as shown with filled circles. As seen from the figure it is possible to fit Δp_h well to the measured data.

The velocity v of the **c**-facet was determined from a linear fit to the middle part of the increasing pressure Δp_h as indicated in Fig. 6 with a dashed line. The driving pressure Δp was obtained during the same time interval, marked with a shaded background in Fig. 6, as an average over the difference $\Delta p_g - \Delta p_h$, i.e., over the gap between the fitted Δp_h and the measured points. Typically we measured and averaged over ten cycles. The variation of both the pressure and the velocity, obtained during different cycles, was typically less than 5%. The accuracy of the fits according to Eq. (36) was improving with a growing drive and with increasing temperature, because the bulge in the driving pressure Δp became more prominent. For example, at $T = 200$ mK the variation of the pressure was less than 1% while the variation of the velocity was less than 2%.

3.4. Velocity Measurement of **a**-Facets

The crystal used for the **a**-facet studies was the same as in the **c**-facet measurements having the **c**-axis parallel to gravity. The crystal was melted so that its edge was seen in the field of view of our CCD-camera. In this orientation **a**-facets are seen from the side as straight parts of the crystal edge. No interference lines were obtained from the **a**-facets.

The speed of the facet can be measured by tracking the position of the facet edge as a function of time in this configuration. At temperatures below 20 mK, the images were obtained every 7.2 seconds while at higher temperatures they were taken with the time interval of $\Delta t = 3.8$ s. The length of the illuminating pulse was 15 ms. The image was recorded using a VHS-video recorder connected to the monitor output of our digital camera. During the time interval between successive snapshots the video output shows the previous image which is stored in the memory of the camera controller. Thus, the recording consists of a semi-continuous video updated after a new image has been acquired. This video recording had a resolution and sensitivity good enough for tracing the edge which was seen as a clear black line. However, one should notice that the video signal, corresponding to an 8-bit grayscale at most, is not good enough for reproducing the interference lines used in the **c**-facet measurements.

The position of the facet edge was determined from a still picture on the monitor. The measurement was made with the help of a millimeter scale on the screen. The position was read with an accuracy of 0.5 mm on the monitor corresponding to a position of the **a**-facet with $25 \mu\text{m}$ error. This method was found accurate enough since the quality of the video

recording was the limiting factor and digitization of the image did not increase the accuracy.

3.5. Addition of ^3He Impurities

Our measurements on crystal growth were performed using regular, commercial ^4He with the nominal purity of 10^{-7} . In order to check the effect of ^3He impurities we added first 0.5 cm^3 of ^3He (NTP) corresponding to about 10 ppm. Later the amount of impurities was increased to 50 ppm by inserting 2.0 cm^3 more of ^3He . The extra ^3He was inserted to the ballast volume while the cryostat was cold since we wanted to keep the same crystal seed as in the measurements with regular ^4He . This ensured that we were able to compare the properties of exactly similar crystals before and after the insertion of additional ^3He . As seen in the results of Sec. 4.4, the addition of a small amount of ^3He made a big difference in the growth properties of our crystals.

The main problem was to get ^3He impurities down the filling line to superfluid ^4He . Once ^3He has reached the superfluid phase, the impurities are expected to move to the experimental volume relatively fast due to the “heat flush” effect. To achieve this we first reduced the size of the crystal to get as much ^4He gas as possible to the room temperature ballast volume which contained the added ^3He . Next we warmed the ballast by about 40°C , thereby driving 300 cm^3 of gas (NTP) from the ballast volume to the filling capillary. We estimate that about 250 cm^3 of gas (NTP) should go through the filling line over to the superfluid phase inside the pot heat exchanger. Repeating this procedure about 10 times we should get most of the ^3He transferred to superfluid ^4He .

One should bear in mind that we were not able to measure directly the concentration of ^3He in the sample cell. Hence, the given concentrations should be considered as rough estimates, not exact figures. As pointed out by Rolley *et al.*,³³ a large amount of ^3He atoms may reside trapped on vortex cores inside the sintered silver heat exchanger. In our experiments the ratio of the cell volume to the sinter area is close to that of Ref. 33 and similar modification of the impurity concentration can be expected. Using a mean distance of 3 nm between ^3He atoms inside vortex cores we estimate that nominal impurity concentrations up to 0.4 ppm can be fully absorbed by our silver sponge. Hence, our original 0.1 ppm purity may be strongly reduced whereas the higher concentrations should be practically uninfluenced. Another problem is of course the distribution of impurities in the liquid phase. Since ^4He superfluid moves towards warmer areas, thermal gradients can change the distribution of ^3He between the different

parts of the filling line, the heat exchanger inside the nuclear stage, and the sample cell.

3.6. Techniques with Small Crystals

We studied the shape of the *c*-facet in crystals either partly or in some cases completely detached from the cell walls. It turned out that the presence of a crystal edge in the image decreased the quality of our pictures, and especially the contrast of the interference lines obtained from the *c*-facet. This was due to the strongly curving part at the crystal edge which produced some very bright and dark areas in the image. Since the dynamic range of the camera is restricted and the interference pattern is weak, it is difficult to get interference lines with strong contrast. Hence, the observations on the shape of the *c*-facet were difficult to make with good accuracy. This situation is clearly different from our earlier measurements on the facet edge³⁴ because in those measurements the rough surface curved only by a few milliradians from the facet while in the present case the edge of the crystal bends about 100 times more.

Some observations were also made on small crystals without any contact with the walls. Typically, it was very difficult to get a crystal detached from the walls. We tried to do this by tilting the whole cryostat. Unfortunately, this process often produced some vibrations resulting in abrupt pressure changes in the filling line and the crystal was destroyed. The easiest way was to nucleate a new crystal and then try to drop it in the middle of the cell. One has to remember, however, that we were able to observe optically only an area with a diameter of about 6 mm while the diameter of the sample cell was 17 mm. Thus, sometimes the crystal might have been out of wall contact but it was not possible to verify this. Small crystals were also difficult to maintain for longer times since pressure fluctuations in the cell could easily destroy them or make them bigger, restoring a contact to the wall. Therefore, we managed only a couple of times to make brief observations on crystals located completely in the field of view of our interferometer.

For static measurements at the lowest temperatures we used long exposure times to reduce the heat leak caused by the absorbed light. The observations on small crystals were typically made with light pulses on the order of 100 s at a 10^{-4} times weaker intensity of the illumination. This should be compared with the usual 15 ms illumination pulses, applied once every second in the dynamic measurements. Assuming that the energy ΔQ absorbed during the exposure is the same, the heat leak \dot{Q} is reduced by a factor of 10^2 when using light pulses of 100 s.

4. EXPERIMENTAL RESULTS

4.1. Nucleation and Orientation of Crystals

Our crystals were nucleated at 20 mK, in contrast to the commonly used temperature of 0.9 K.³⁵ No external electrical fields were employed to enhance the pressure locally. A typical nucleation event is shown in Fig. 7. Before time t_0 , the crystal melts at the melting pressure p_0 with a gas flow of $\dot{n} \approx -10 \mu\text{mol/s}$. The crystal vanishes at $t=t_0$, and at $t=t_1$ the flow to the ballast volume is stopped. This is enough to start to increase the pressure in the cell, since the cold gas evaporated in the filling line warms and expands. The overpressure $p-p_0$ increases owing to the feed $\dot{n}=1 \mu\text{mol/s}$ till the value p_2 at $t=t_2$ when the nucleation occurs, leading to an abrupt drop in pressure down to a level p_1 . This jump $\delta p = p_2 - p_1 \sim 3.5 \text{ mbar}$ is the overpressure required for the nucleation of a new crystal; the value is close, but slightly smaller than those observed in previous experiments on nucleation pressures.^{36,37} The hydrostatic pressure difference between levels p_0 and p_1 indicates that the new crystal nucleates 10 mm above the bottom of the cell. Finally, at $t=t_3$, the crystal has become big enough to drop to the bottom of the sample cell resulting again in the pressure p_0 .

The nucleation site was history dependent: If the pressure was dropped more than $\sim 0.8 \text{ bar}$ below the melting pressure, the next crystal was nucleated at a new site. A statistical analysis was made on the nucleation pressures. It was discovered that the pressures increased with decreasing temperature down to 100 mK. Below 100 mK no temperature dependence

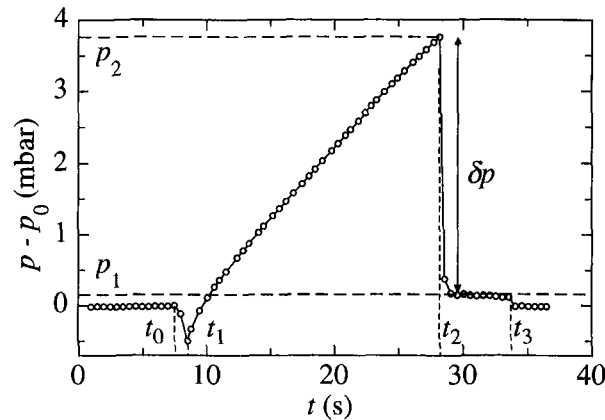


Fig. 7. Nucleation of a ^4He -crystal. See text for details.

was seen. Together with a statistical analysis of the distribution of pressures this suggests that the nucleation process is governed by quantum tunneling at low temperatures. A description of the study on nucleation pressures has been published elsewhere.³⁸

Crystals were aligned with their c-facet almost parallel to the reference surface of the optical wedge by nucleating and dropping crystals until a suitable one was obtained. Normally it took around 20 attempts to get a crystal with the c-facet close enough to the orientation of the reference surface to see interference lines. Once there was a suitable crystal seed on the bottom, it was grown slowly ($1\ \mu\text{m/s}$) sideways to cover the whole cross-section of the sample cell.

4.2. Growth of c-Facets Without Screw Dislocations

To our surprise, the growth of our freshly-nucleated crystals produced pressure traces which could not be explained by spiral growth. Figure 8 displays the behavior of the pressure in the sample cell when the c-facet grew at 20 mK. The pressure increases almost linearly up to some instability value and then drops fast about $100\ \mu\text{bar}$ in less than 1 sec. This pressure drop corresponds, according to the compressibility of the liquid, to the growth of the facet by 200–2000 layers.

It is obvious that this kind of pressure trace cannot be due to spiral growth in which the pressure should first increase to a threshold level (see Eq. (9)) and then stabilize to a value depending on the growth rate in the experiment; in Fig. 8 the expected pressure would be below $1\ \mu\text{bar}$. We

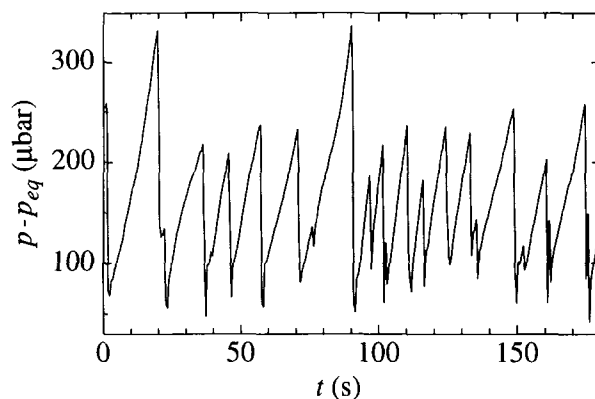


Fig. 8. Deviation of pressure p from the equilibrium p_{eq} as a function of time t during growth of a high-quality crystal ($\bar{v} = 170\ \text{nm/s}$).

were able to decrease the overpressure dramatically for the facet growth by producing a few dislocations above 200 mK as described in Sec. 4.3. Thus it seems reasonable to argue that our crystals did not contain any screw dislocations along the *c*-axis after the nucleation.

The absence of an electrical field together with the low nucleation temperature was probably the reason why crystals without screw dislocations along the *c*-axis could be obtained in our experiments. It is quite possible that the nucleation capacitors, ordinarily used to enhance the liquid pressure locally, produce inhomogeneous electric fields which give rise to a small number of dislocations in the nucleating seed. On the other hand, the small dissipation and the large interfacial mobility at our nucleation temperature of 20 mK certainly contribute to the formation of homogeneous, dislocation-free crystals.

4.2.1. Slow Growth

During the sections of increasing pressure between the instability points in Fig. 8, we discovered a slow, continuous movement of interference lines using the Fourier method described in Sec. 3.2. In order to study this slow growth regime quantitatively, we measured the average velocity using a constant pressure drive which was accomplished by actively controlling the heating of the room temperature ballast volume. Figure 9 shows traces of displacement Δh of the facet obtained at two different driving pressures at $T = 50$ mK. The fitted lines correspond to velocities $v = 8.9 \cdot 10^{-2}$ nm/s ($\Delta p = 370$ μ bar) and $v = 2.8 \cdot 10^{-2}$ nm/s

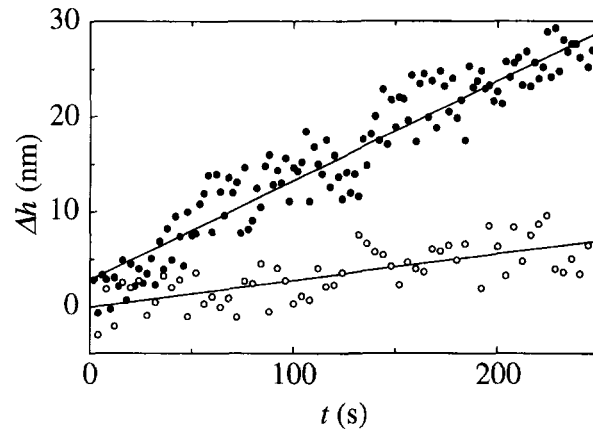


Fig. 9. Vertical displacement Δh of a growing *c*-facet as a function of time t at $T = 50$ mK, measured at the driving pressure of $\Delta p = 370$ μ bar (●) and $\Delta p = 200$ μ bar (○).

($\Delta p = 200 \mu\text{bar}$). Note that the standard deviations of the fitted lines from the data are 3 nm and 2 nm, respectively.

The rate of the slow growth as a function of pressure is illustrated in Fig. 10. Each point in the figure represents a $\Delta h(t)$ measurement illustrated in Fig. 9. The measured speeds of the c-facet vary between 0.01 nm/s–0.6 nm/s. The highest applicable pressures were limited by the instability points. As can be noticed from Fig. 10, the velocities are decreasing with increasing temperature. The scatter of the slow growth data comes partly from the difficulty in regulating the overpressure at a fixed level and partly from the linear fit. The pressure values in Fig. 10 were obtained as averages of Δp over the total imaging time of the interference lines. Typical pressure fluctuations were about $\pm 10\%$ of the average value.

It is difficult to distinguish the functional shape of the v vs. Δp -plots of the slow growth. There seems to be a certain resemblance with the corresponding plots of the spiral growth which display a crossover from Δp^2 dependence to Δp dependence (see Sec. 4.3). Within our accuracy, however, it is possible to make always linear fits using the equation

$$v = \mu_f a(\Delta p/\rho_l) \Delta p \quad (37)$$

where μ_f defines a mobility for the slow growth. Using this linear approximation we obtain the mobility as a function of temperature T as

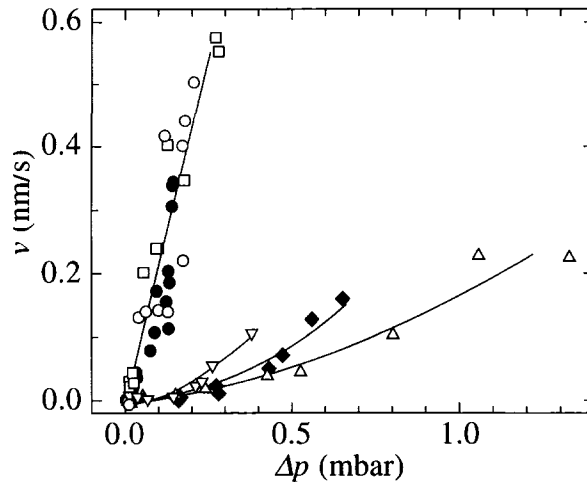


Fig. 10. Slow growth of the c-facet without screw dislocations. Temperatures: $T = 2 \text{ mK}$ (\circ), 10 mK (\square), 20 mK (\bullet), 50 mK (∇), 100 mK (\blacklozenge), and 200 mK (\triangle). Solid lines are for guiding the eyes.

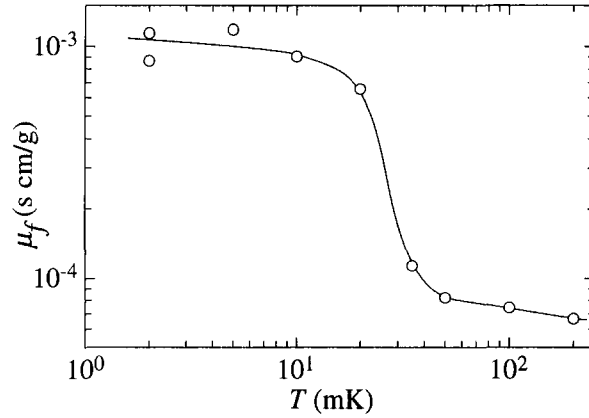


Fig. 11. Mobilities μ_f of the slow growth obtained from linear fits to the data of Fig. 10. The solid curve is for guiding the eyes.

shown in Fig. 11. The mobility μ_f decreases by about a factor of ten when temperature increases from 2 mK up to 200 mK.

The theoretical explanation of the slow growth is largely open. One clue can be the similarity to the spiral growth data (compare Fig. 10 with Fig. 18) even though the velocities of the two growth modes differ by many orders of magnitude. In both cases the low temperature data below 50 mK seem quite linear while at higher temperatures quadratic behavior is followed more or less. One possibility is some kind of a surface reconstruction which could provide exceedingly massive and less mobile steps instead of the normal ones. According to Eq. (15) this would decrease the speed of a step.

4.2.2. Burst-Like Growth

In contrast to the slow growth, the crystal can grow by creating new atomic layers abruptly in a burst-like manner as illustrated by the p vs. t trace in Fig. 8. This kind of behavior with distinct instabilities takes place at average velocities $v > 1$ nm/s when the crystal is growing at a fixed rate of mass flow.

Figure 12 shows cumulative distributions of instability pressures at eight different temperatures between 2 and 250 mK. The instability pressures are sorted from the smallest to the biggest and then their ordinal number is plotted as a function of the pressure; thus the distributions indicate the number of instability events below the pressure Δp . The burst-like growth depends strongly on temperature, as Fig. 12 shows. The distributions were

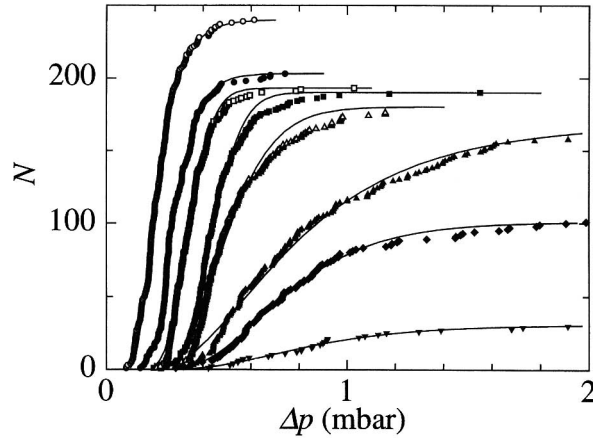


Fig. 12. Cumulative distributions of instability pressures of the burst-like growth. Temperatures from left to right are 2 mK, 50 mK, 100 mK, 150 mK, 180 mK, 200 mK, 210 mK, and 250 mK. See text for solid lines.

measured with the average interfacial velocity of 200–300 nm/s, but no variation as a function of speed was observed in the range 100–600 nm/s.

It is possible to fit the overall shape of the pressure-dependent, statistical nucleation formula to the measured data.³⁸ Assuming a linear pressurization rate $\Delta p(t) \sim ct$ one obtains the cumulative distribution

$$N = N_0 \left[1 - \exp \left(- \int_0^{\Delta p} \frac{w(\Delta p)}{c} d(\Delta p) \right) \right] \quad (38)$$

where N_0 is the total number of nucleation events. The nucleation rate $w(\Delta p)$ is of the form $w \propto \exp(-B_q/\Delta p^2)$ in quantum nucleation and $w \propto \exp(-B_t/\Delta p)$ in the thermal case.^{39, 40} Within our experimental accuracy, both formulas can be fitted rather well to the data; for example, the solid curves in Fig. 12 are fits of Eq. (38) using the quantum nucleation rate. As seen from the figure, the curves seem to fit the data quite well suggesting some kind of nucleation mechanism behind the burst-like growth. Note that the measured temperature dependence of the nucleation pressure is opposite to that expected for thermal nucleation. This is why we prefer the formulas of quantum nucleation to those of thermal activation in our fit.

The magnitude of the instability pressures and the asymmetry of their distributions in Fig. 12 are growing with temperature. The circles in Fig. 13

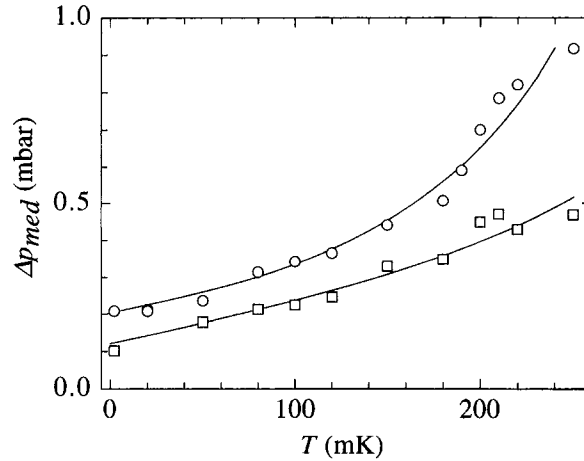


Fig. 13. The median instability pressure (○) of the burst-like growth as a function of temperature. The squares (□) show the median pressure after the nucleation of new layers. Solid lines are for guiding the eyes.

show the median value of these distributions as a function of temperature. The median overpressure increases by a factor of four with the increasing temperature from 20 mK up to 250 mK. Above 250 mK we were not able to obtain enough data since the pressurization quickly resulted in an overpressure $\Delta p > 3$ mbar which created screw dislocations along the *c*-axis on the facet, destroying the burst-like growth mode.

Another characteristic feature of the burst-like growth is that the restabilization pressure, i.e., the value of Δp at which the rapid nucleation of new layers ends, depends strongly on temperature as well. The restabilization pressures form a symmetric distribution which is fairly close to an integral error function as shown in Fig. 14. The symmetric distributions are in clear contrast to those of the instability pressure (see Fig. 12). This suggests that the pressure after the abrupt growth is governed by a random process. The distributions become wider at higher temperatures. The median pressure is also increasing with the temperature by a factor of five as shown in Fig. 13.

The understanding of restabilization pressures is somewhat complicated by the clear undershoot in pressure, seen before the linear increase is regained (see Fig. 8). The time scale of the undershoot ($\tau \sim 0.5$ s) is much longer than what we would expect for sound waves in our experimental setup ($\tau \sim 1$ ms). The data presented in Fig. 14 has been obtained by neglecting the undershoot in the analysis.

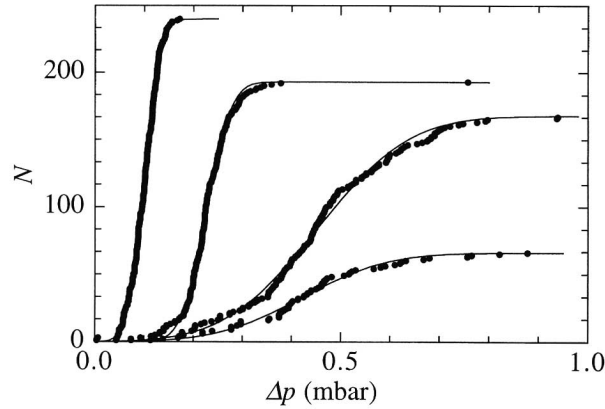


Fig. 14. Cumulative distributions of the pressure after the burst-like creation of new layers. The temperatures from left to right: $T = 2$ mK, 100 mK, 200 mK, and 220 mK. The solid curves are fits of integral error function.

4.3. Spiral Growth

Spiral growth was investigated in crystals with a small density of dislocations ($n_s = 5\text{--}100\text{ cm}^{-2}$). Dislocations were generated by growing the crystal horizontally at a few hundred $\mu\text{m/s}$ or vertically at about $1\ \mu\text{m/s}$ at $T \sim 200$ mK. The creation of dislocations was seen as a dramatic drop in the overpressure Δp down to about $1\ \mu\text{bar}$, which corresponds to the threshold of the spiral growth with a small density of dislocations. Moreover, it was possible to eliminate the dislocations by melting the crystal below its size in the original creation process, thereby restoring the burst-like and slow growth modes.

Figure 15 shows an example how the growth threshold is observed during sinusoidal growth and melting on one of our crystals. In the beginning there is a region marked with S where no movement of the interference lines is observed. When the overpressure reaches $2\ \mu\text{bar}$ the lines start to move indicating growth of the facet just above the threshold. This threshold pressure stays the same during the periodic growth and melting, which means that the number of dislocations doesn't change during our growth rate measurements.

To infer numerical values for the threshold we have employed the minimum pressure during one period as the reference pressure p_{eq} . Within our resolution this value coincides with the equilibrium pressure. Using Eq. (9) one obtains that the smallest (largest) measured threshold $0.5\ \mu\text{bar}$ ($2\ \mu\text{bar}$) corresponds to a density of dislocations $n_s = 5\text{ cm}^{-2}$ (100 cm^{-2}).

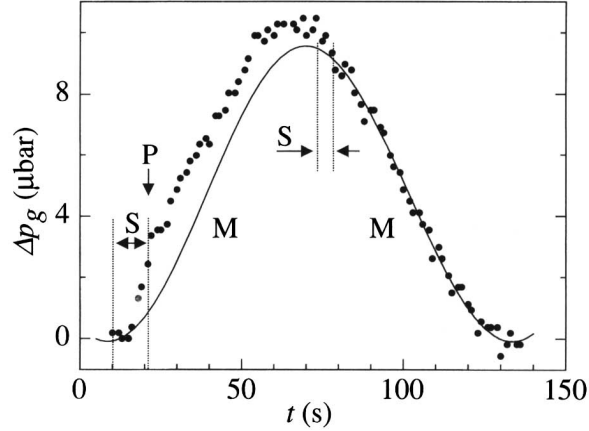


Fig. 15. The pressure in the cell during one period of sinusoidal growth and melting of the c-facet measured at $T = 20$ mK in a crystal with $n_s = 50 \text{ cm}^{-2}$. Regions of motion (M) and of non-motion (S) of the facet are inferred from 32×32 pixel snapshots. At point P the interface starts to move indicating that the threshold pressure of the spiral growth has been exceeded. The amplitude of the facet movement is 0.5 mm . The solid line is a fit of Δp_h according to Eq. (36).

The minimum value is smaller by an order of magnitude than the previously reported densities.^{12,41} However, one has to bear in mind that the measurement of the growth threshold might be less sensitive to the density of other defects in the crystal, e.g., edge dislocations.

Figure 16 illustrates how the movement of the interference lines is easily seen from the interferograms. In the upper row there is a series of images of the size 32×32 pixels taken with the time interval of $\Delta t = 0.93 \text{ s}$ at $T = 20 \text{ mK}$. The lower row shows images obtained by subtracting two successive frames of the upper row. The subtraction of the first and the second frame shows no lines, meaning that the interference fringes and the c-facet have not moved between the snapshots. However, between the second and the third frame of the upper row the lines have shifted which is seen as a set of fringes in the subtracted image.

The difference between the measured pressure Δp_g and the fitted hydrostatic pressure Δp_h (see Fig. 15) depends strongly on the speed of the c-facet and on the temperature. Figure 17 shows pressure traces measured at $T = 100 \text{ mK}$ with six different amplitudes of oscillation corresponding to facet velocities $v = 8\text{--}74 \text{ }\mu\text{m/s}$. With increasing drive the threshold is exceeded sooner which is seen as the movement of the curves to the left. Since the bulge due to the difference between Δp_g and Δp_h increases with

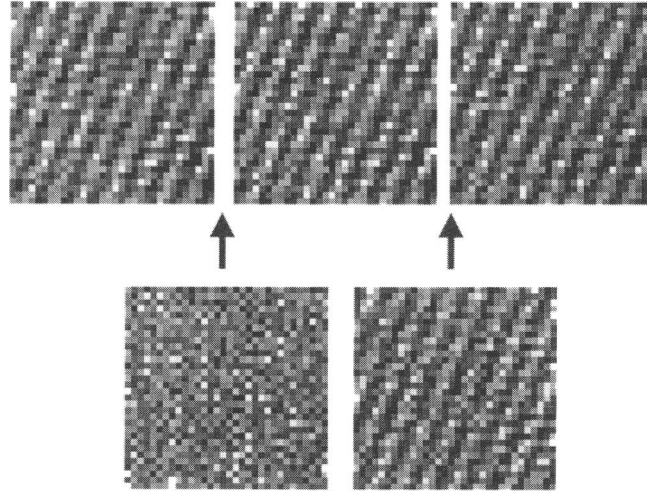


Fig. 16. Upper row shows 32×32 pixel images taken with the time interval $\Delta t = 0.93$ s. Lower row shows images obtained by subtracting two successive frames of the upper row. In the first image on the lower row there are no interference lines, while the second subtraction contains visible fringes indicating that the facet has started to move between second and third frame of the upper row.

the drive, it is easier to measure the velocity and the corresponding driving pressure at large speeds.

Figure 18a shows the velocity v of a *c*-facet as a function of overpressure Δp at different temperatures. The data of Fig. 18a between $T = 100$ – 200 mK can be fitted quite well with the classical Δp^2 -dependence up to velocities $30 \mu\text{m/s}$ by using Eq. (14) with a double-step. In contrast, at lower temperatures $T \leq 20$ mK the pressure dependence is almost linear. In both cases there appear deviations at high velocities from the small speed behavior. These effects are explained in the theoretical part (see Sec. 2.2.2) on the basis of the theory for spiral growth which takes into account the mass of steps and the localization of kinks. We obtain from our low temperature data, using Eq. (20), a step mass of $m = 4$ – $5 \cdot 10^{-18}$ g/cm which is in a good agreement with the theoretical value $m = 5$ – $7 \cdot 10^{-18}$ g/cm.^{20,42,43} The solid lines in Fig. 18a are fits of Eqs. (15) and (17) obtained using μ_0 as a fitting parameter at constant $\eta = 4.3 \cdot 10^2$ and $m = 5 \cdot 10^{-18}$ g/cm. As seen from the figure our new theory on spiral growth is able to explain all our experimental data. This is also supported by the good agreement between the obtained step mobility and the theoretically calculated value (see below).

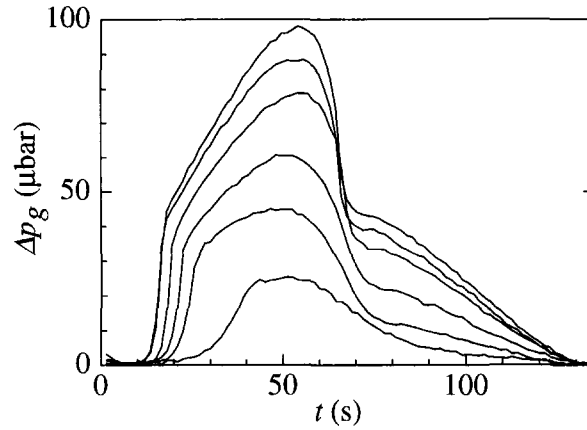


Fig. 17. Pressure Δp_g during periodic growth and melting of the c-facet shown at different oscillation amplitudes at $T = 100$ mK. Notice the enhancement in the size of the bulge indicating an increase in the driving pressure Δp . The threshold pressure is $\Delta p_c = 0.5 \mu\text{bar}$.

Of special interest is the value of η which is closely connected, according to Eq. (16), to the basic characteristics of elementary kinks, *viz.* the width of their energy band Δ_k . Assuming the density of kinks to be of atomic order, $n_k \approx 10^7 \text{ cm}^{-1}$, we obtain an estimate $\Delta_k \approx 10 \text{ K}$ which looks quite reasonable in view of other, essentially quantum properties of the liquid-solid helium interfaces (see, e.g., Refs. 1 and 44).

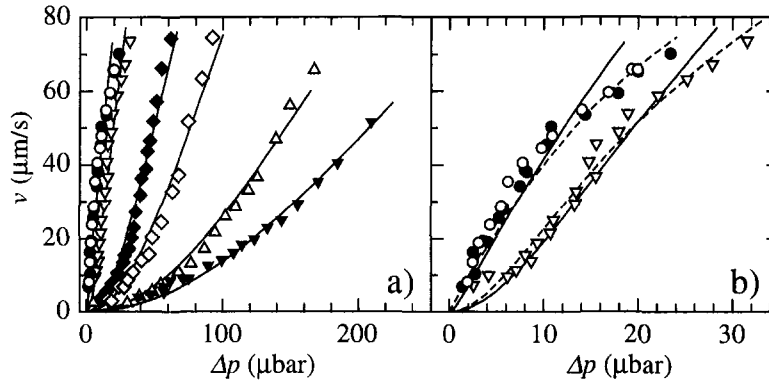


Fig. 18. (a) Velocity v of the c-facet as a function of the driving pressure Δp for a crystal with the dislocation density $n_s = 5 \text{ cm}^{-2}$: $T = 2 \text{ mK}$ (\circ), 20 mK (\bullet), 50 mK (∇), 100 mK (\blacklozenge), 150 mK (\diamond), 200 mK (\triangle) and 250 mK (\blacktriangledown). (b) An expanded view of the low temperature data. The symbols are the same as in (a). See text for the solid and dashed lines.

The velocity data at $T = 2\text{--}50$ mK are shown in Fig. 18b on an expanded scale. Deviations from the theoretical fits (solid curves) are quite strong at high growth rates and at low temperatures. It is possible to make better fits if η is increased. The dashed lines in Fig. 18b show fits obtained using η as a fitting parameter: $\eta = 960$ at $T = 20$ mK and $\eta = 750$ at $T = 50$ mK. Similarly, it is possible to make better fits at higher temperatures using $\eta < 400$. Such a temperature variation of η , if it really exists, looks quite natural from the point of view of the theory in Sec. 2.2.2: In the beginning of the regime of localization, the step is not as “hot,” as it is assumed in Eq. (16), and first with increasing temperature of the phonon bath the average energy of quasiparticles becomes large enough ($\sim \Delta_k$).

The tendency towards saturation supports the interpretation based on the step inertia, since in the case of Cherenkov radiation the facet velocity should grow linearly. However, the deviation between solid curves and the data at low temperatures may also be due to the heating of the sample caused by the large speed of crystallization during the measurements. A moving interface introduces a heat production rate

$$\dot{Q} = \frac{\Delta p}{\rho_l} S v \Delta p \quad (39)$$

where Δp is the pressure over the interface and S is the surface area of the facet. Using the values $v = 50 \mu\text{m/s}$ and $\Delta p = 10 \mu\text{bar}$ one obtains $\dot{Q} = 1$ nW. This is large compared with the thermal conductivity of the tube connecting the sinter and the optical cell at low temperatures (see Sec. 3.1). Assuming that the mechanical work done by the moving interface is completely irreversible and that the heat goes to the liquid, one finds that the sample warms up from 2 to 7 mK during such a motion. Thus the sample is expected to warm up at large amplitudes of oscillation leading to deviations from the theoretical curve. At high temperatures, the thermal conductivity of the liquid increases and the heat leak due to the moving interface is not significant any more. This is why we prefer to use in the analysis of the experimental data just an average value of η instead of a temperature dependent function, which doesn't seem to be very reliably determined under our experimental conditions.

The step mobility μ_0 is shown in Fig. 19 as a function of temperature. This was obtained from the calculated fits to the data shown in Fig. 18a. Figure 19 displays also the step mobility measured by Rolley *et al.*¹² on a vicinal surface with the inclination angle $\theta = 0.3^\circ$. The solid curve is a fit to data points of the form $\mu_0 \sim 1/T^n$ with the exponent $n = 3.04$ which is close to the value $n = 3.5$ obtained by Rolley *et al.*¹² at 0.1–0.2 K; our mobilities are, however, a factor of five smaller than theirs.

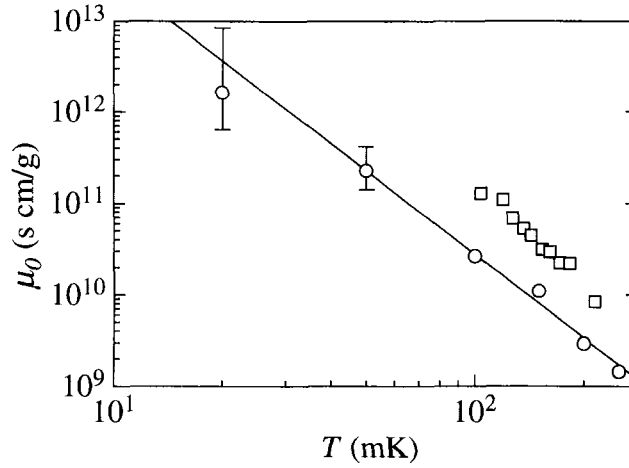


Fig. 19. Mobility μ_0 (○) as a function of temperature T obtained using μ_0 as a fitting parameter in Eqs. (15) and (17) with $\eta = 430$ and $m = 5 \cdot 10^{-18}$ g/cm. The solid line is a fit of $\mu_0 \propto 1/T^n$ where $n = 3.04$. The mobility obtained by Rolley *et al.* for a vicinal surface with 0.3° inclination angle is shown by open squares.

The temperature dependence of μ_0 is due to the scattering of thermal phonons from moving steps. In a winding spiral, the spacing of the arms d is much larger than λ , the wavelength of thermal phonons. In this case, the phonons are scattered incoherently from the steps and the mobility becomes $\mu_0 \propto 1/T^3$; for coherent scattering $\mu_0 \propto 1/T^4$.²⁰ Taking into

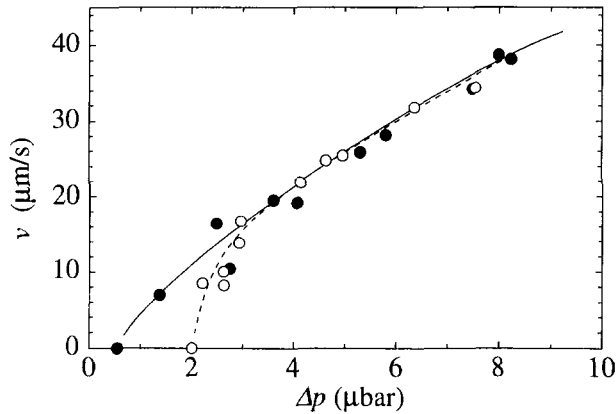


Fig. 20. Velocity v of the e-facet as a function of the driving pressure Δp at $T = 20$ mK for a crystal with (●) 5 dislocations/cm² and (○) 50 dislocations/cm². The points at $v = 0$ show the threshold pressures obtained from the interferometric measurements. The solid and dashed lines are for guiding the eyes.

account the uncertainty of the data points at the lowest temperatures, the measured exponent $n = 3.04$ is in an excellent agreement with the expected, incoherent scattering with $n = 3$. The absolute values of the mobility at temperatures 100–200 mK, where it was measured with higher accuracy, agree well with theoretical estimations.²⁰

The measurements on the spiral growth were mainly done at our smallest dislocation density of 5 cm^{-2} , but some data were taken also at a higher density. Figure 20 illustrates the v vs. Δp plots measured at $T = 20 \text{ mK}$ in crystals having 5 and 50 dislocations per cm^2 . The figure shows that, as expected, only the threshold is changing since the speed of spiral growth is governed by the winding rate around the individual dislocations.

4.4. Effect of ^3He Impurities

In order to check the role of ^3He impurity atoms on our growth phenomena, especially on the slow growth of facets in the absence of screw dislocations, we investigated samples where the amount of ^3He impurities was increased by a factor of 100/500 with respect to the initial natural purity. Typically, the presence of ^3He impurities slows down interfacial growth rates.⁴⁵ This was also the case in our measurements. Figure 21 illustrates the effect of impurities on the slow growth at $T = 20$ and 200 mK

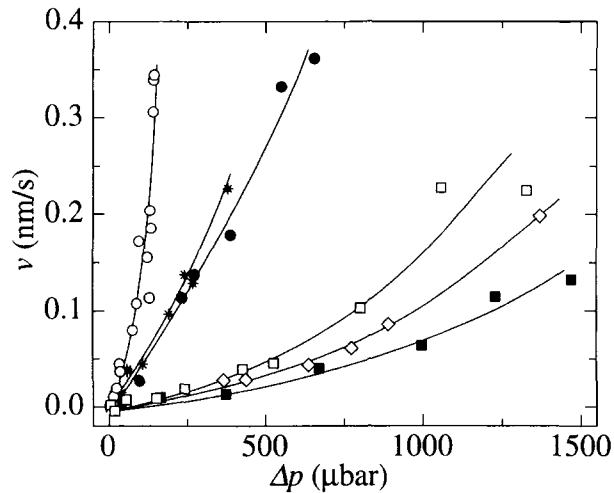


Fig. 21. The effect of ^3He impurities on the slow growth at $T = 20 \text{ mK}$ with 0.1 ppm (\circ), 10 ppm ($*$) and 50 ppm (\bullet) of ^3He and at $T = 200 \text{ mK}$ with 0.1 ppm (\square), 10 ppm (\diamond) and 50 ppm (\blacksquare). Solid lines are just to guide the eyes.

over the concentrations $c_3 = 0.1, 10$ and 50 ppm. The overall effect is to decrease the growth rate by a factor of three.

At $T = 20$ mK the increase of c_3 from 0.1 ppm to 10 ppm was responsible for most of the effect. However, at $T = 200$ mK, the increase of c_3 from 0.1 ppm to 10 ppm yielded roughly a similar change as that when c_3 is further increased to 50 ppm. At $T = 20$ mK the whole change was slightly bigger than at 200 mK. On the basis of these results we may conclude that the presence of ^3He atoms does not seem to lead to impurity assisted growth processes where the impurity atoms on the facets would act as nucleation centers for new atomic layers.

The effect of impurities on the burst-like growth at $T = 20$ mK and 200 mK is illustrated in Fig. 22; the cumulative distributions of instability pressures have been scaled between 0 and 1 . At both temperatures the distributions are shifted towards higher pressures with increasing ^3He concentrations. At 20 mK the increase of the median pressure was 40% with the change of the impurity concentration from $c_3 = 0.1$ ppm to 10 ppm and 80% up to $c_3 = 50$ ppm. At 200 mK the corresponding figures were 60% and 250% from the original median pressures. Thus, it is clear that an enhanced amount of impurities is detrimental for the burst-like growth.

Altogether, the effect of ^3He impurities is to slow down all the growth modes investigated in this paper. This is similar to the studies of the growth resistance on rough surfaces by Wang and Agnolet.⁴⁵ As in their work, the sensitivity of interfacial mobility on the amount of ^3He impurities increases with decreasing temperature. Hence, it would be very interesting to use ultrapure ^4He for studying different growth mechanisms of *c*-facets at the

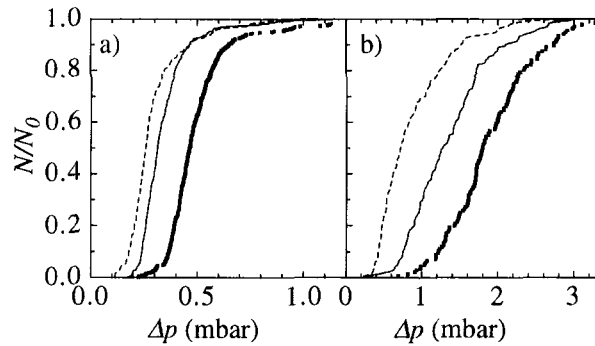


Fig. 22. Cumulative distributions of the burst-like growth scaled between 0 and 1 at three different ^3He impurity concentrations. Dashed lines show the distributions with the nominal ^3He concentration of $c_3 = 0.1$ ppm, solid thin lines with $c_3 = 10$ ppm and the filled squares with $c_3 = 50$ ppm at (a) $T = 20$ mK and (b) $T = 200$ mK.

lowest temperatures. Moreover, since the spiral growth provides an almost ideal geometry, i.e., well separated steps moving at a relatively large speed, systematic investigations of the spiral dynamics in the presence of ^3He impurities might offer a good way to characterize both the step-impurity interactions as well as the structure of the steps themselves.

4.5. Growth of a-Facets

We studied the growth of **a**-facets by measuring the position of vertically oriented facets. Figure 23 shows two examples of such crystals imaged at $T=2$ mK and 200 mK. A thin white line can be noted in Fig. 23a just above the crystal edge which is seen as a thick black line. This white strip is the contact line of the crystal to the bottom window. Typically the contact line was seen during the **a**-facet measurements, which indicates that the facet was not touching the bottom. However, at large driving pressures and at high temperatures, when the mobility of the **a**-facet was smaller, the contact line got closer to the crystal edge as the radius of curvature of the rough part became smaller. Under these conditions the contact line was not visible any more as shown in Fig. 23b except at the corners where two **a**-facets meet.

The growth of **a**-facets was measured by increasing the heating of the ballast volume step-wise and monitoring the position of the facet edge and the pressure of the cell. Figure 24 shows the position of the facet edge as a function of time during growth at $T=2$ mK. A linear fit to the data yielded the velocity of the facet while the driving pressure was obtained as an average over the tracing of the edge.

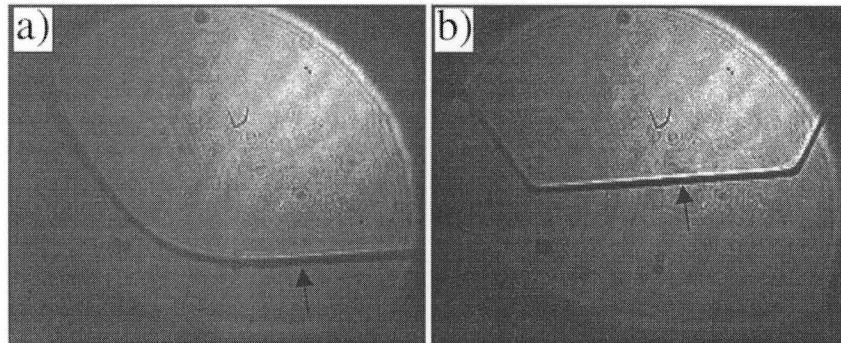


Fig. 23. Edge of a ^4He -crystal during growth showing two/three **a**-facets from the side: (a) $T=2$ mK with $\Delta p=3 \mu\text{bar}$ and $v=18 \mu\text{m/s}$ and (b) $T=200$ mK with $\Delta p=31 \mu\text{bar}$ and $v=11 \mu\text{m/s}$. The arrows indicate the **a**-facet monitored for the v vs. Δp -plot. The light area is the illuminated part of the sample cell. The frame size is $7 \times 6 \text{ mm}^2$

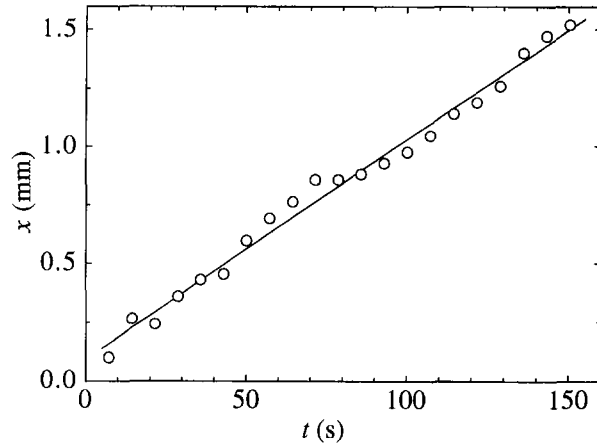


Fig. 24. Position x of the **a**-facet as a function of time t measured at $T=2$ mK with the driving pressure $\Delta p = 3.5 \mu\text{bar}$. The solid line is a linear fit yielding the velocity of the facet $v = 9.4 \mu\text{m/s}$.

Figure 25 shows v versus Δp curves at different temperatures measured for the **a**-facet. Even though the facets are now vertical and their properties, like the step height and the step energy, are different from those of the **c**-facets, we have tried to analyze our data by employing the same formulas and parameters as in the case of **c**-facets. The solid lines are fits calculated from Eqs. (15) and (17) for the spiral growth with $m = 5 \cdot 10^{-18}$ g/cm which corresponds to the average of the values $m = 2 - 8 \cdot 10^{-18}$ g/cm, obtained

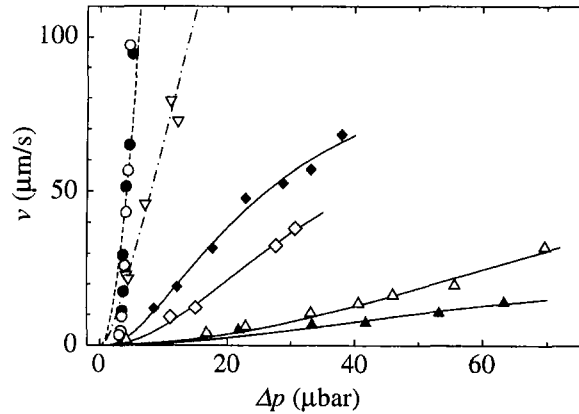


Fig. 25. Velocity v of the **a**-facet as a function of the driving pressure Δp measured at $T=2$ mK (\circ), 20 mK (\bullet), 50 mK (∇), 100 mK (\blacklozenge), 150 mK (\diamond), 200 mK (\triangle) and 250 mK (\blacktriangle). See text for the curves.

using the mass as a free fitting parameter. Note that this is exactly the same value as measured for the c-facet. However, it was not possible to make a good fit below 50 mK with $m = 5 \cdot 10^{-18}$ g/cm. The fit at 50 mK, marked as a dash-dotted line, was made using $m = 2 \cdot 10^{-18}$ g/cm. The fit at 20 mK, indicated by the dashed line, was obtained with $m = 2 \cdot 10^{-20}$ g/cm but even then the fit to the data was not good at low velocities.

Figure 26 shows the mobilities μ_0 of steps obtained from the fits of Fig. 25 as a function of temperature. Mobility seems to saturate at low temperatures but this may also be a result of the small mass used in the fit. The solid line indicates a fit to mobilities at $T = 50$ –250 mK giving $\mu_0 \sim 1/T^n$ with the exponent $n = 3.5$. This value is close to that obtained on the c-facet.

One can understand the above results taking into account that the vertical orientation of the a-facets introduces a new factor to the growth: the hydrostatic pressure is now changing along the facet. We were not able to measure the thickness of the crystal directly, but we may estimate the crystal height to be on the order of the capillary length $h \sim 1$ mm. Using this value, one obtains a hydrostatic pressure difference $\Delta p_{\text{hyd}} \sim 10$ μbar across the facet. The step motion becomes much more complicated with such an extra force. Since Δp_{hyd} is on the order of the driving pressure used in the measurements below 50 mK, the theory of Sec. 2.2.2 is not applicable to these data. At higher temperatures a typical driving pressure becomes

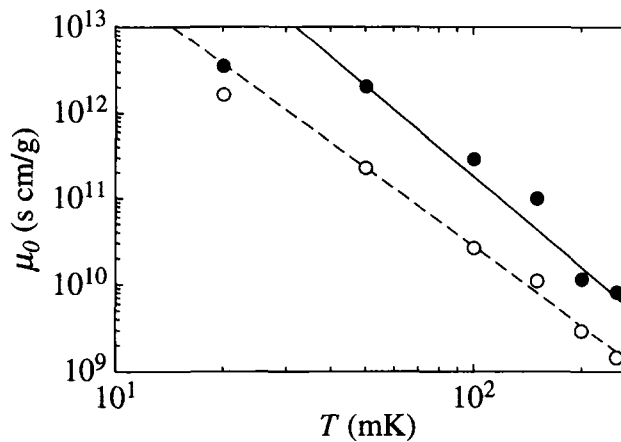


Fig. 26. Mobility μ_0 for steps on an a-facet (●) obtained from the fits in Fig. 25. Solid line is a fit to the points at $T = 50$ –250 mK yielding $\mu_0 \sim 1/T^{3.5}$. The open circles (○) are the mobilities obtained for the c-facet (see Fig. 19). The dashed line indicates the fit $\mu_0 \sim 1/T^{3.04}$ to the c-facet data.

larger than the hydrostatic pressure difference $\Delta p \gg \Delta p_{\text{hyd}}$ and, consequently, the gravitational effects are not important any more.

The threshold for the spiral growth of **a**-facets was not determined as accurately as in the case of **c**-facets, since now the start of the facet growth with respect to increasing pressure was not determined using interferometric fringes. An extrapolation of the data of Fig. 25 to zero growth rate yields for the threshold $\sim 3 \mu\text{bar}$. This is several times larger than the value observed for the **c**-facet. However, it can be shown that, in the presence of Δp_{hyd} , the threshold for spiral growth exceeds its regular value by a fraction of Δp_{hyd} which is dependent on the position of the dislocation on the facet. On the other hand, the typical size of a stationary **a**-facet ($\sim 1 \text{ mm}$) was quite small when compared with the size of a **c**-facet ($\sim 15 \text{ mm}$). Thus, it is possible that the facet does not even contain a single dislocation in a good quality crystal. The facet has to expand first sideways in order to reach a screw dislocation. With these notions, the increased value of the threshold for the **a**-facet seems reasonable.

4.6. Shape of a **c**-Facet at Low Temperatures

We tried to observe “freezing” of kinks by monitoring the facet edge down to our minimum temperature, about 2 mK. This was performed with a crystal partly detached from the side wall. Figure 27 shows a typical image on an equilibrium crystal with the background subtracted away.

The crystal edge consists of two **a**-facets which are joined by a rounded section. The crystal in Fig. 27 is different from the crystal used for the growth measurements, which can be seen from the altered orientation of the interference fringes (compare with Fig. 16). Our interferograms did not show any clear changes in the shape of the **c**-facet. No obvious sharpening of the facet corner was seen, which should take place if the anisotropy energy of steps due to the kink energy would be essential (see Sec. 2.1). In general, the facet edge seemed to follow the shape of the crystal edge, both along the **a**-facets and along the curved corner.

Figure 28 shows the ratio B/A of the distances between the facet border and the crystal edge in the middle of the **a**-facet and at the corner of the crystal, marked in Fig. 27 by (B) and (A), respectively. The sharpening of the facet edge should be seen as an increase of B/A . However, the measured ratio only decreases slightly when the temperature is lowered. The ratio starts to increase above $T = 0.9 \text{ K}$ because the **a**-facets disappear.

We made optical observations also on small crystals without any contact to the walls of the sample cell. These crystals stuck quite easily to the bottom of the cell. This was seen as a distortion of the crystals from their hexagonal shape. Bigger crystals, with the diameter of $\sim 3 \text{ mm}$ or more,

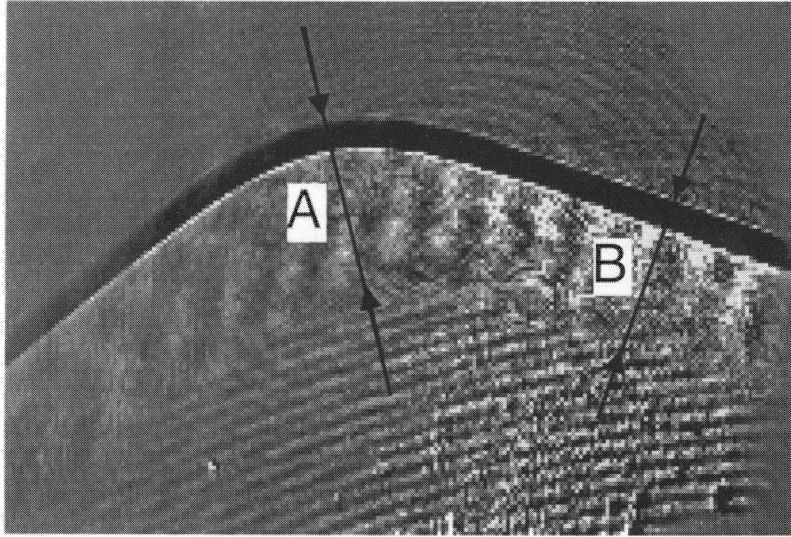


Fig. 27. Image, measured at $T = 2$ mK, shows a c-facet near the crystal edge at a place where two a-facets meet. The shape of the c-facet follows the general shape of the crystal; curvature of the interference fringes on the facet is due to bending of the reference plate. The distance between the crystal edge and the facet border has been marked with arrows at the corner of the crystal (A) and in the middle of a straight crystal edge (B). The ratio B/A is shown in Fig. 28 as a function of temperature.

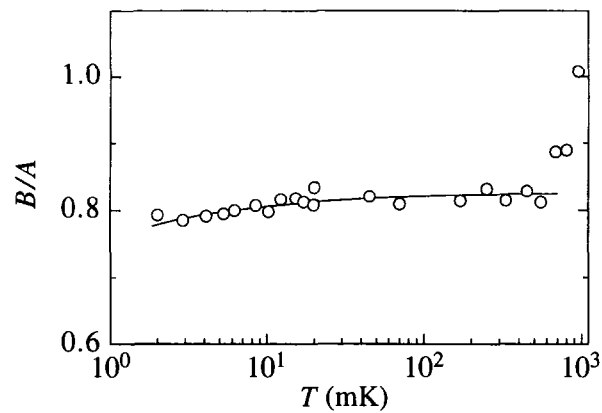


Fig. 28. Ratio B/A of the distances between the c-facet border and the crystal edge as specified in Fig. 27. Above $T \approx 0.9$ K the ratio $B/A \rightarrow 1$ because the corner of the crystal becomes rounded owing to the vanishing of a-facets. The solid line is for guiding the eyes.

were more symmetric, possibly due to stronger influence of vibrations which prevented them from sticking. The monitoring of interference lines of the c-facet was even more difficult than in the case of a crystal partly on the wall due to the reasons mentioned in Sec. 3.6. The general shape of the facets in our small crystals down to 2 mm in diameter appeared to be an elongated ellipse which varied with the degree of sticking on the bottom. No changes in the symmetry of the facet could be resolved, which could be regarded as an indication of the freezing of kinks in our experiments.

4.7. Search for Supersolid and New Faceting Transitions

The pressure of the sample was monitored down to our minimum temperature in order to observe anomalies connected with the supersolid transition (see Eq. (26)). The crystal was partially detached from the side wall in order to damp external pressure fluctuations by exposing extra rough surface to the liquid. The small increase of pressure in the filling line due to boiling of the He-bath was compensated with a gradually-cooled room temperature ballast volume.

Figure 29 shows the change in the capacitance of our pressure gauge ΔC vs. the temperature T of the nuclear stage during a slow warm-up. We did not observe any anomalies connected with the supersolid transition along the lines of Eq. (26). The melting pressure stayed constant within an accuracy of $\Delta p \sim 0.5 \mu\text{bar}$ between 2–8 mK. Our pressure sensitivity is 40 times better than the value of 2 Pa reported by the Leiden group who

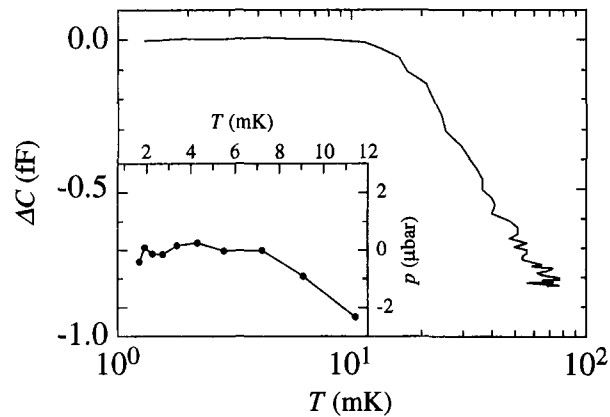


Fig. 29. Change in the capacitance of the pressure gauge ΔC vs. temperature T of the nuclear stage during a slow warm-up. The zero of the capacitance is fixed to the level measured at the lowest temperature. The inset shows a blow-up of the pressure below 12 mK.

measured the melting pressure between 1.5–120 mK.⁴⁶ Assuming that $T_c = 1$ mK,⁴⁶ we obtain an upper limit for the concentration of zero point vacancies, $x_v < 5 \cdot 10^{-7}$, which is slightly smaller than the value $x_v < 6 \cdot 10^{-7}$ reported by the Leiden group.

The measured capacitance decreases fast above 10 mK. The melting curve is expected to decrease only by $3 \mu\text{bar}$ due to the phonon contribution between 1 mK and 100 mK,⁴⁶ which corresponds to a decrease in the capacitance by 0.2 fF. The extra decrease of the measured curve is probably due to changes in the dielectric constant in the unshielded sections of the electrical wiring which connects the gauge with the capacitance bridge.

During the course of the measurements described in this paper we kept an eye on possible indications of new faceting transitions, such as the appearance of new interference fringes near the crystal edge. No such discoveries were made. This does not, however, rule out the possibility of new transitions between 2–70 mK since our optical system is not very good for this kind of measurements due to its small field of view and the small angular resolution. The particular orientations of the crystals employed in our experiments made it difficult to observe efficiently other orientations than those of the **c**- and **a**-facets.

5. SUMMARY AND CONCLUSIONS

In our work we have extended the minimum temperature of optical studies on ^4He crystals down to 2 mK. Several new findings, connected with crystal nucleation and growth, were obtained. By nucleation of crystals at $T = 20$ mK without external electric fields, we were able to obtain crystal seeds which did not contain any screw dislocations along the **c**-axis. These seeds could be transformed into crystals with dislocation densities $\sim 10 \text{ cm}^{-2}$ by growing them rapidly at 200 mK, while melting of the crystals back to their original size eliminated the defects.

Our investigations on the growth of **c**-facets with dislocation densities $5\text{--}50 \text{ cm}^{-2}$ agree well with the classical parabolic power law for spiral growth at $T = 100\text{--}200$ mK. However, a linear dependence on the driving pressure is observed at 2–20 mK, which is due to the inertia of elementary steps in a rapidly turning spiral. Step velocities on the spiral reach values of ~ 100 m/s, i.e., about to the maximum possible value. At the highest velocities, a slight tendency to saturation is observed, which suggests that the limit of step localization is approached at large driving forces.

The step mobility extracted from the spiral growth measurements follows a $1/T^{3.04}$ -law, which is in a good agreement with the theoretical picture of independent steps whose mobility is limited by the kink-phonon

scattering.²⁰ The obtained values are also in good agreement with the results of Rolley *et al.*¹² who measured the step mobility on vicinal surfaces at inclination angles >0.3 degrees.

The studies of **a**-facets yielded results similar to those obtained for the spiral growth of **c**-facets. The results remained more qualitative, mostly because of the complications caused by the varying hydrostatic pressure along a vertical facet.

No effects due to the freezing of kinks on the shape of facets could be resolved down to 2 mK. The absence of this effect seems natural in the light of the observed high-mobility steps at the same temperature. Such steps could not exist if the density of kinks on the steps were to decrease exponentially with temperature.

In crystals void of screw dislocations, the growth was found to be intriguing. Contrary to expectations such crystals displayed slow, continuous facet growth up to speeds 0.5 nm/s; at higher speeds the growth became discontinuous. Both growth modes become more effective with decreasing temperature. Hence, the **c**-facet is able to grow even in the absence of the usual spiral growth at low temperatures.

The apparent interfacial mobility of the slow growth mode is about one million times smaller than the mobility observed in spiral growth. Such a small mobility is puzzling in the light of the present theoretical models. In our previous work, moreover, we found that the equilibrium shape of a ⁴He crystal contains an unexpected surface state transition from a regular vicinal plane to a state governed by $1/\theta$ -dependent surface stiffness.³⁴ At the moment, it is not clear how these static and dynamic properties are interweaved. We believe that the slow growth mode has to be somehow connected with the observed curvature of facets. The ability to link the dynamic and static properties of the interface better together would also make the identification of the new surface state much easier.

The growth of defect-less crystals becomes jump-like at rates >1 nm/s, and 200–2000 layers are formed abruptly in one burst. In general, the instability pressures of the bursts form distributions which fit rather well with the ordinary activation behavior of creating new atomic layers. However, the temperature and pressure dependencies of the results make them rather challenging to account for fully.

Altogether, only the spiral growth of our ⁴He crystals is well understood. Even in this case, the interpretation involves a small factor of doubt. In our experiments it is difficult to distinguish truly between Cherenkov radiation and step inertia, because of the similarities in the functional forms of the respective mobilities. Slight tendency towards saturation in the facet velocity is observed, which lends support to the latter interpretation. In order to make a more proper distinction further measurements are

necessary, for example, by extending the experiments to larger velocities and driving pressures, thereby probing deeper into the nonlinear region of the step mobility. Another possibility is to add ^3He impurities to the sample. If the Cherenkov-radiation is the dominant mechanism, then no change should take place when increasing the amount of ^3He atoms. Experimental work to check this point is presently underway. In addition, interesting phenomena have been predicted⁴⁷ in the presence of ^3He impurities due to the existence of a bound state^{33, 48} at the liquid solid interface.

ACKNOWLEDGMENTS

We want to thank A. Andreev, S. Balibar, O. Lounasmaa, M. Paalanen, J. Penttilä, E. Rolley, J. Saramäki, E. Sonin, and V. Tsymbalenko for useful discussions and comments. This work was supported by the Academy of Finland and by the Human Capital and Mobility Program ULTI of the European Union.

REFERENCES

1. K. O. Keshishev, A. Ya. Parshin, and A. I. Shal'nikov, *Soviet Scientific Reviews, Section A: Physics Reviews*, Vol. 4, I. M. Khalatnikov (ed.), Harwood Academic, New York (1982), p. 155.
2. S. G. Lipson and E. Polturak, in *Progress in Low Temperature Physics*, Vol. XI, D. F. Brewer (ed.), Elsevier Science Publishers B.V., Amsterdam (1987), p. 127.
3. P. Nozières, in *Solids Far From Equilibrium*, C. Godrèche (ed.), Cambridge University Press, Cambridge (1991), p. 1.
4. K. O. Keshishev, A. Ya. Parshin, and A. V. Babkin, *Zh. Eksp. Teor. Fiz.* **80**, 716 (1981) [*Sov. Phys. JETP* **53**, 362 (1981)].
5. M. J. Graf and H. J. Maris, *Phys. Rev. B* **35**, 3142 (1987).
6. O. A. Andreeva, K. O. Keshishev, and S. Yu. Osep'yan, *Pis'ma Zh. Eksp. Teor. Phys.* **49**, 661 (1989) [*JETP Lett.* **49**, 759 (1989)].
7. C. L. Wang and G. Agnolet, *Phys. Rev. Lett.* **69**, 2102 (1992).
8. E. Rolley, E. Chevalier, C. Guthmann, and S. Balibar, *Phys. Rev. Lett.* **72**, 872 (1994).
9. P. E. Wolf, F. Gallet, S. Balibar, E. Rolley, and P. Nozières, *J. Phys. (France)* **46**, 1987 (1985).
10. F. Gallet, S. Balibar, and E. Rolley, *J. Phys. (France)* **48**, 369 (1987).
11. V. L. Tsymbalenko, *Fiz. Nizk. Temp.* **21**, 162 (1995) [*Sov. J. Low Temp. Phys.* **21**, 120 (1995)].
12. E. Rolley, C. Guthmann, E. Chevalier, and S. Balibar, *J. Low. Temp. Phys.* **99**, 851 (1995).
13. J. P. Ruutu, P. J. Hakonen, A. V. Babkin, A. Ya. Parshin, J. S. Penttilä, J. P. Saramäki, and G. Tvalashvili, *Phys. Rev. Lett.* **76**, 4187 (1996).
14. S. Balibar and B. Castaing, *J. Phys. Lett. (France)* **41**, 329 (1980).
15. J. E. Avron, L. S. Balfour, C. G. Kuper, J. Landau, S. G. Lipson, and L. S. Schulman, *Phys. Rev. Lett.* **45**, 814 (1980).
16. P. E. Wolf, S. Balibar, and F. Gallet, *Phys. Rev. Lett.* **51**, 1366 (1983).
17. A. F. Andreev and A. Ya. Parshin, *Zh. Eksp. Teor. Fiz.* **75**, 1511 (1978) [*Sov. Phys. JETP* **48**, 763 (1978)].
18. M. Uwaha and P. Nozières, *J. Phys. (France)* **48**, 407 (1987).

19. W. K. Burton, N. Cabrera, and F. C. Frank, *Phil. Trans. Roy. Soc.* **243**, 299 (1951).
20. P. Nozières and M. Uwaha, *J. Phys. (France)* **48**, 389 (1987).
21. K. R. Atkins and R. A. Stasior, *Can. J. Phys.* **31**, 1156 (1953).
22. See, e.g., L. Esaki, *Physica Scripta T* **42**, 102 (1992), and references therein.
23. V. I. Marchenko and A. Ya. Parshin, *Zh. Eksp. Teor. Fiz.* **79**, 257 (1980) [*Sov. Phys. JETP* **52**, 129 (1980)].
24. A. F. Andreev and I. M. Lifshitz, *Zh. Eksp. Teor. Fiz.* **56**, 2057 (1969) [*Sov. Phys. JETP* **29**, 1107 (1969)].
25. G. V. Chester, *Phys. Rev. A* **2**, 256 (1970).
26. For a recent review, see M. W. Meisel, *Physica B* **178**, 121 (1992).
27. Star 1-camera, manufactured by Photometrics, Tucson, Arizona, USA.
28. G. C. Straty and E. D. Adams, *Rev. Sci. Instr.* **40**, 1393 (1969).
29. Andeen-Hagerling 2500A, Andeen-Hagerling, Inc., Cleveland, Ohio 44139-2231, USA.
30. J. Wilks, *The Properties of Liquid and Solid Helium*, Oxford University Press, Oxford (1967).
31. S. Kostianovski, S. G. Lipson, and E. N. Ribak, *Appl. Opt.* **32**, 4744 (1993).
32. IPLab image processing software for Macintosh, Signal Analytics Corp., 440 Maple Avenue East, Vienna, Virginia 22180, USA.
33. E. Rolley, S. Balibar, C. Guthmann, and P. Nozières, *Physica B* **210**, 397 (1995).
34. A. V. Babkin, H. Alles, P. J. Hakonen, A. Ya. Parshin, J. P. Ruutu, and J. P. Saramäki, *Phys. Rev. Lett.* **75**, 3324 (1995).
35. A. V. Babkin, D. B. Kopeliovich, and A. Ya. Parshin, *Zh. Eksp. Teor. Fiz.* **89**, 2288 (1985) [*Sov. Phys. JETP* **62**, 1322 (1985)].
36. S. Balibar, B. Castaing, and C. Laroche, *J. Phys. Lett. (France)* **41**, 283 (1980).
37. V. L. Tsymbalenko, *J. Low Temp. Phys.* **88**, 55 (1992).
38. J. P. Ruutu, P. J. Hakonen, J. S. Penttilä, A. V. Babkin, J. P. Saramäki, and E. B. Sonin, *Phys. Rev. Lett.* **77**, 2514 (1996).
39. A. F. Andreev, *Progress in Low Temperature Physics*, Vol. VIII, D. F. Brewer (ed.), Elsevier Science Publishers B.V., Amsterdam (1982), p. 68.
40. M. Uwaha, *J. Low Temp. Phys.* **52**, 15 (1983).
41. G. A. Lengua and J. M. Goodkind, *J. Low Temp. Phys.* **79**, 251 (1990).
42. A. M. Kosevich and Yu. A. Kosevich, *Fiz. Nizk. Temp.* **7**, 809 (1981) [*Sov. J. Low Temp. Phys.* **7**, 394 (1981)].
43. See also J. Amrit, P. Legros, and J. Poitrenaud, *J. Low Temp. Phys.* **101**, 971 (1995).
44. D. O. Edwards, S. Mukherjee, and S. Pettersen, *Phys. Rev. Lett.* **64**, 902 (1990).
45. See, e.g., C.-L. Wang and G. Agnolet, *J. Low Temp. Phys.* **89**, 759 (1992).
46. P. G. van de Haar, C. M. C. M. van Woerkens, M. W. Meisel, and G. Frossati, *J. Low Temp. Phys.* **86**, 349 (1992).
47. A. Ya. Parshin, *J. Low Temp. Phys.*, **110**, 133 (1998).
48. J. Treiner, *J. Low Temp. Phys.* **92**, 1 (1993).